Obscured Active Galactic Nuclei

Ryan C. Hickox[1] and David M. Alexander[2]

[1]Department of Physics & Astronomy, Dartmouth College, Hanover, NH 03755, USA; email: Ryan.C.Hickox@dartmouth.edu
[2]Centre for Extragalactic Astronomy, Department of Physics, Durham University, Durham, DH1 3LE, UK; email: d.m.alexander@durham.ac.uk

Xxxx. Xxx. Xxx. Xxx. YYYY. AA:1–49

https://doi.org/10.1146/((please add article doi))

Keywords

active galaxies, AGN surveys, black holes, central torus, mergers, obscuration

Abstract

Active Galactic Nuclei (AGN) are powered by the accretion of material onto a supermassive black hole (SMBH), and are among the most luminous objects in the Universe. However, the huge radiative power of most AGN cannot be seen directly, as the accretion is "hidden" behind gas and dust that absorbs many of the characteristic observational signatures. This obscuration is an important challenge for uncovering the complete AGN population and understanding the cosmic evolution of SMBHs. In this review we describe a broad range of multi-wavelength techniques that are currently employed to identify obscured AGN, and assess the reliability and completeness of each technique. We follow with a discussion of the demographics of obscured AGN activity, explore the nature and physical scales of the obscuring material, and assess the implications of obscured AGN for observational cosmology. We conclude with an outline of the prospects for future progress from both observations and theoretical models, and highlight some of the key outstanding questions.

Contents

1. Introduction

An AGN is the observed manifestation of gas accretion onto a supermassive black hole (SMBH). In the broadly accepted view of AGN, the accretion of gas around the SMBH produces an optically thick disk of material (termed the "accretion disk"), which emits thermally due to viscosity within the disk (e.g., Shakura & Sunyaev 1973; Rees 1984). The gas within the accretion disk has a wide range of temperatures (with the temperature an inverse function of the distance from the SMBH) and, consequently, the emission is produced over a broad wavelength range (termed the spectral energy distribution; SED).[1] For the accretion disk of a typical AGN, the range of gas temperatures is likely to be T $\approx 10^4$–10^5 K and, therefore, the majority of the emission from the accretion disk will be at $\approx$ 30–300 nm (i.e., at UV–optical wavelengths).

The SED of an AGN accretion disk is distinct from that of other astrophysical sources, making them comparatively easy to identify; see **Figure 1** for the different SEDs between a star-forming galaxy and the accretion disk. This is fortuitious since the accretion disk is small and unresolved for even the closest and brightest AGN (i.e., light hours–light days in physical size). The accretion of gas onto a SMBH is an exceptionally efficient process ($\approx$ 5–42% of the mass is ultimately converted into emission, depending on the spin of the

[1]We note that this model may only be appropriate for high-accretion rate AGN (typical $L/L_{\rm Edd} > 10^{-3}$), which are the focus of this review. See Done, Gierliński & Kubota (2007) and Yuan & Narayan (2014) for discussions of low-accretion rate systems.

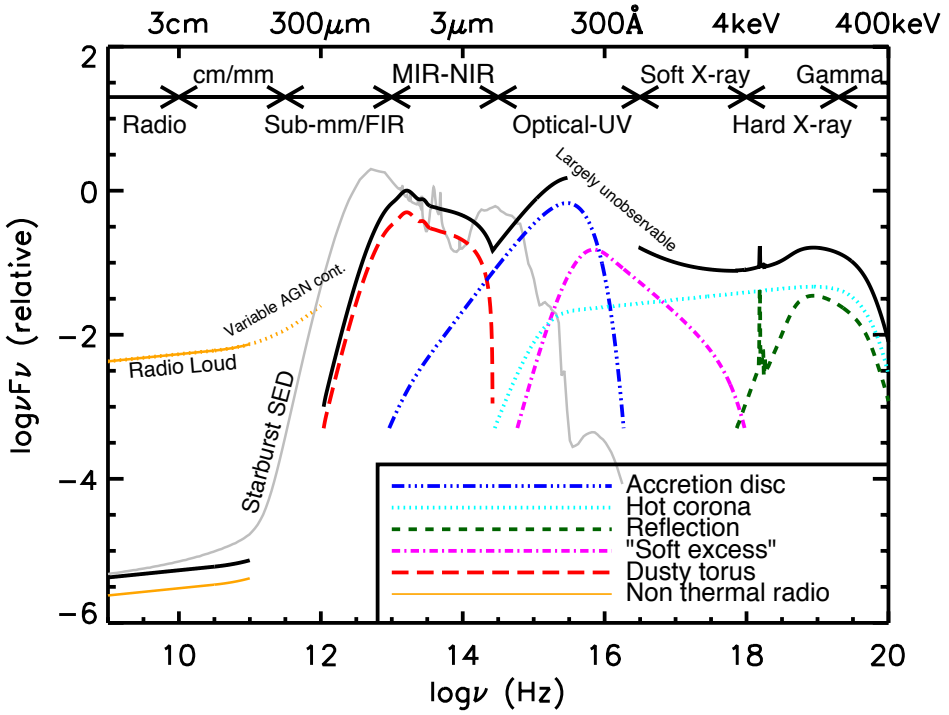

Figure 1

Schematic representation of the spectral energy distribution (SED) of an unobscured AGN (black curve), separated into the main physical components (as indicated by the colored curves) and compared to the SED of a star-forming galaxy (light grey curve). Figure from Harrison (2014), courtesy of C. M. Harrison.

SMBH; e.g., Kerr 1963; Shapiro & Teukolsky 1983) and therefore large luminosities can be produced for a modest amount of accretion, allowing for luminous AGN to be detected out to high redshifts. Indeed, luminous AGN are the most powerful non-explosive objects in the Universe.

The first systematic studies of AGN occured over 50 years ago and led to the definition of some of the main classes (e.g., Seyfert 1943; Baade & Minkowski 1954; Schmidt 1963): Seyfert galaxies, radio galaxies, and quasars. It is not the objective of this review to describe the menagerie of different AGN classes, which has been extensively covered in Padovani et al. (2017). However, we note that in the current parlence, "Seyfert galaxies" is often used to indicate AGN of low–moderate luminosity ($L_{\rm bol} \approx 10^{42}$–$10^{45}$ erg s^{-1}) while "quasars" is often used to indicate AGN of high luminosity ($L_{\rm bol} > 10^{45}$ erg s^{-1}). $L_{\rm bol}$ is the bolometric luminosity of the AGN, which corresponds to the total luminosity produced (or inferred, for systems where the accretion disk emission is not directly detected) by the accretion disk.

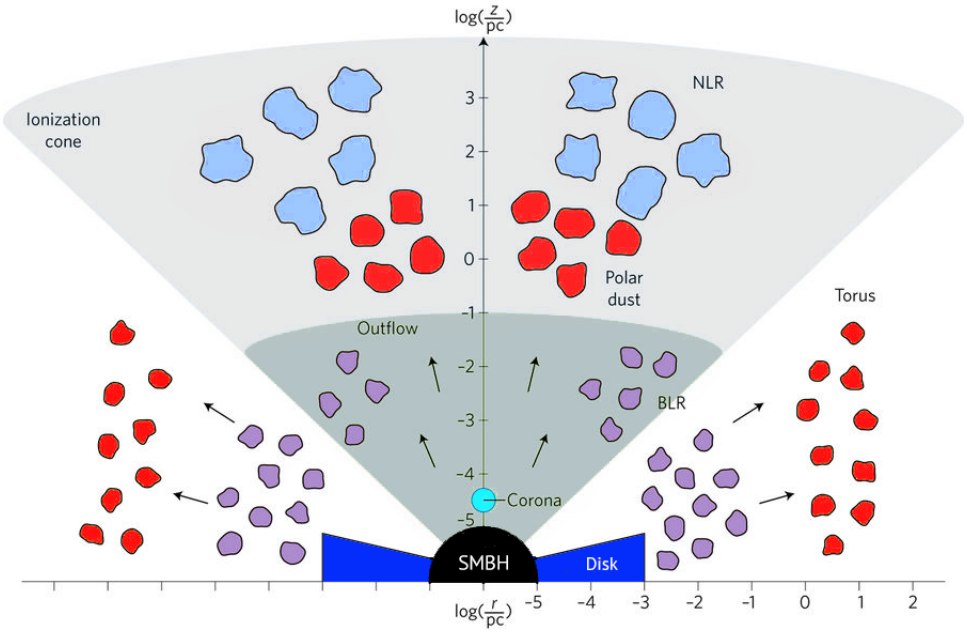

Figure 2

Schematic representation of the AGN physical model, illustrating the broad scales of the key regions. The accretion disc, corona, broad-line region (BLR), and the dusty torus reside within the gravitational influence of the SMBH. The disk, corona, and torus (including polar dust clouds) are colored corresponding to the lines showing their contributions to the SED in Figure 1). The narrow-line region (NLR) is on a larger scale and under the gravitational influence of the host galaxy. Adapted from Ramos Almeida & Ricci (2017), courtesy of C. Ramos Almeida and C. Ricci.

1.1. A brief overview of obscured AGN

The focus of this review is obscured AGN. These are systems where the emission from the accretion disk is not directly detected due to the presence of material between the accretion disk and the observer. In a general sense, obscuration is defined as anything that absorbs emission and/or scatters a large fraction away from the line of sight of the observer. In astrophysical sources the obscuring medium is typically composed of dust and/or gas. Dust is the common term used to describe solid-state structures, which are typically carbonaceous grains and amorphous silicate grains (see Draine 2003a for a review). Gas is the term used to describe a broad range of gaseous states, from fully ionised gas, including electrons and protons, to neutral gas and molecular compounds. Dust dominates the source of obscuration at UV–infrared (IR) wavelengths, while gas dominates the absorption at X-ray energies. However, the impact of the obscuring material on the detection of the accretion-disk emission is dependent on wavelength. Physically this is referred to as the optical depth, which is the product of the opacity and density of the material (κ_λ; ρ) and the path length (s); for example, see Rybicki & Lightman (1986) for a general overview. A low optical depth indicates that a small fraction of the emission will be absorbed while a high optical depth implies the converse.

For many (probably the majority of) obscured AGN, the obscuration occurs in the close

vicinity of the accretion disk and lies within the gravitational influence of the SMBH. In the favoured picture for the physical structure of AGN (termed the "unified model" of AGN ; e.g., Antonucci 1993; Urry & Padovani 1995; Netzer 2015), the accretion disk is surrounded by a geometrically and optically thick dusty and molecular "torus" (often referred to as the "dusty torus"); see **Figure 2** for a schematic of the AGN physical model from Ramos Almeida & Ricci (2017). The torus is expected to be within the gravitational influence of the SMBH and could be considered, in a broad sense, the cool outer regions of the accretion disk where molecules and dust grains can form. The anisotropic nature of the torus means that for some lines of sight the accretion-disc emission is directly detected while for others it is obscured by the dust and gas within the torus. However, the obscuration can also come from the host galaxy (e.g., from dust-obscured star-forming regions; dust lanes) and is likely to be more significant for inclined and edge-on galaxies and for galaxies in gas-rich mergers since, on average, the typical optical depth along a given line of sight will be higher than for face-on normal galaxies (e.g., Goulding et al. 2012; Buchner & Bauer 2017).

In addition to the accretion disk and torus there are two other key regions that we consider in this review for the identification of AGN: the broad line region (BLR) and the narrow line region (NLR). The BLR and NLR are defined based on the velocity width of the detected emission lines in AGN. Empirically, the BLR contains gas with a broader distribution of velocities than the NLR; the velocity width of the NLR is often constrained from the forbidden emission lines since the gas density in the BLR is too high for forbidden transitions. The typical range of velocity widths for the gas in the BLR is $\approx$ 1,000–10,000 km s^{-1} while for the NLR it is $\approx$ 100–500 km s^{-1} (e.g., Padovani et al. 2017). The different velocity widths of the BLR and the NLR are due to the relative location of the gas with respect to the SMBH. The gas in the BLR lies within the gravitational influence of the SMBH and, consequently, resides close to the accretion disk and is typically undetected in obscured AGN; see **Figures 2–3**. By comparison, the NLR gas lies under the gravitational influence of the host galaxy (e.g., Ho 2009) and is produced on larger scales. The bulk of NLR emission generally originates within the central kpc (e.g., Humphrey et al. 2015; Villar-Martín et al. 2016), but for some systems emission from gas ionized by the AGN is observed on the scale of the entire galaxy, out to $\sim$10 kpc (e.g., Liu et al. 2013; Hainline et al. 2013, 2014). Due to its extent, the NLR emission will generally not be obscured by the torus, although a large fraction of the emission could be obscured by dust in the galaxy.

The classical definition of an obscured AGN is the absence of emission from the BLR in the optical waveband (e.g., Antonucci 1993). This corresponds to a typical obscuring screen (or "extinction") from dust of $\approx$ 5–10 mags (typically defined in the V-band at 550 nm; i.e., $A_{\rm V}$ = 5–10 mag; e.g., Burtscher et al. 2016; Schnorr-Müller et al. 2016). For typical dust-to-gas ratios (e.g., as measured in the Galaxy; Predehl & Schmitt 1995) this corresponds to an equivalent absorbing column density from gas measured in the X-ray band of $N_{\rm H} > 10^{22}$ cm^{-2}. The NLR can be detected in both obscured and unobscured AGN while the BLR is only expected to be detected in unobscured AGN; see **Figure 3**.

The absence of direct emission from the accretion disk makes obscured AGN more challenging to identify than unobscured AGN for two key reasons:

1. diminished emission: the obscuring material reduces, and in extreme cases completely extinguishes, the emission from the AGN
2. host-galaxy dilution: the emission from other physical processes in the galaxy (e.g., the emission from starlight or star formation) dilutes or overwhelms the diminished emission from the AGN, in extreme cases making the system indistinguishable from

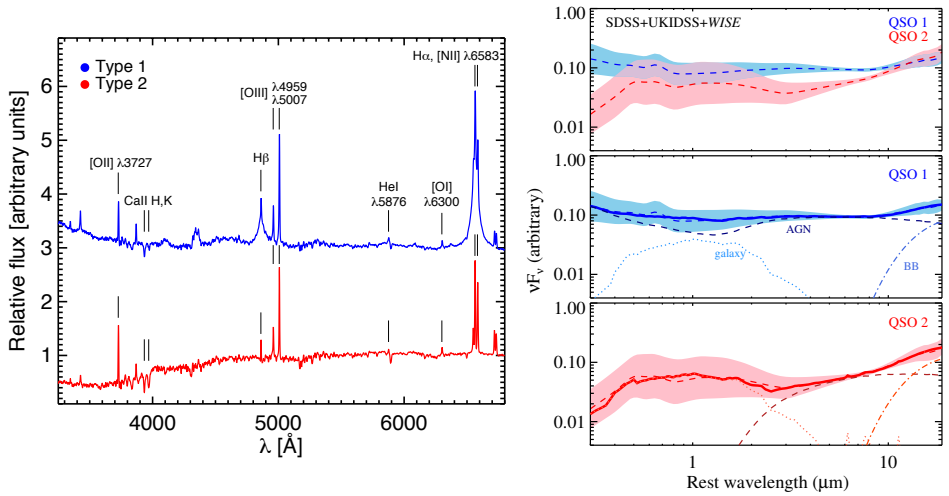

Figure 3

(Left) Composite optical spectrum of Type 1 (blue) and Type 2 (red) AGN from SDSS, adapted from DiPompeo et al. (2018), with the prominent emission lines highlighted. The primary differences between the spectra are the presence of bluer nuclear continuum and (by definition) broad permitted emission lines in the Type 1 AGN, while similar narrow AGN lines are observed in both spectra. (Right) Composite optical–MIR SEDs of Type 1 and Type 2 quasars selected from SDSS, using data from SDSS, UKIDSS, and *WISE* (Hickox et al. 2017). The composite SEDs are modeled with contributions from a (reddened) AGN (dashed lines), the host galaxy (dotted lines), and an empirical blackbody component representing emission from cooler dust (dot-dashed lines). The SEDs are dramatically different in the optical due to reddening of the AGN continuum, but are very similar in the mid-IR, highlighting the power of mid-IR observations to select obscured AGN.

that of a galaxy

The impact of these two effects is dependent on the wavelength, the amount of obscuration, and the relative ratio of the observed emission from the AGN and the host galaxy. This is illustrated in **Figure 4**, which shows schematic multi-wavelength images and SEDs for an AGN plus the host galaxy for varying levels of nuclear obscuration (parameterized by the hydrogen column density $N_{\rm H}$) and the strength of the AGN emission relative to the host galaxy (given by the fraction of the intrinsic emission from the AGN at 1 μm, $f_{\rm AGN}$). It is immediately clear that some AGN signatures are heavily suppressed due to obscuration or dilution from the host-galaxy emission, while others remain visible; however the precise observability of these signatures depends on many parameters including the AGN luminosity and the shape of its intrinsic spectrum, the characteristics of the host galaxy, and the geometry and physical nature of the obscuring material. The wavelength dependent impact of obscuration and host-galaxy dilution on the identification of obscured AGN are discussed in more detail in §2.

1.2. The importance of identifying obscured AGN

The identification of obscured AGN has broad implications for observational cosmology. The majority of the AGN population is obscured and therefore the construction of a complete census of AGN activity requires the identification of both obscured and unobscured sources. A complete census of AGN activity is required to reliably measure the cosmological buildup of SMBHs and to place fundamental constraints on the average radiative efficiency of SMBH growth; we explore this more in Section 5. In the unified AGN model the difference between an obscured and unobscured AGN is the orientation of the dusty torus with respect to the observer. Therefore, in some sense the identification of all obscured AGN may appear to be just a simple book-keeping exercise (i.e., just accounting for the fraction of the AGN population that are obscured and therefore not included in unobscured AGN selection approaches). However, the obscured AGN fraction is found to be a function of AGN luminosity and potentially redshift, and is therefore not simply a single value (see Section 3). Furthermore, obscured AGN are more likely to be found in more dust and gas rich environments than unobscured AGN and, therefore, the lack of a complete census of obscured AGN could give a skewed view of the host-galaxy and larger-scale environments in which AGN reside (see Sections 4 and 5).

This review aims to provide an overview of our observational and theoretical understanding of obscured AGN. In Section 2 we describe the challenges in identifying obscured AGN and assess the effectiveness of the most common techniques, emphasizing two key factors: how reliable and how complete a given technique is for the identification of obscured AGN. In Section 3 we present the overall demographics of obscured AGN activity. In Section 4 we discuss the physical nature of obscuration in AGN and consider the relative contributions of obscuration from the nuclear torus, nuclear starburst regions, and structures on the scale of the host galaxy. In Section 5 we assess the implications of obscured AGN for observational cosmology and explore the significance of obscured AGN for SMBH–galaxy growth and the cosmological radiative efficiency of SMBH growth. Finally in Section 6 we summarise our conclusions and discuss the prospects for future observations and theoretical models to advance the study of obscured AGN. We note that due to space limitations we have had to be selective in our choice of cited articles and we apologize in advance for the many significant studies that we have been been unable to include. We encourage the reader to also consult the following complementary reviews on the identification of AGN, the co-evolution of AGN and galaxies, and the unified model of AGN: Ho (2008), Alexander & Hickox (2012), Heckman & Best (2014), Brandt & Alexander (2015), Netzer (2015), Padovani et al. (2017), and Ramos Almeida & Ricci (2017).

2. Identification of Obscured AGN

In this section we give an overview of the variety of methods commonly used to identify and characterize obscured AGN. We have divided this section into separate sub sections to correspond to the various wavebands used to identify obscured AGN: UV–near-IR (0.1–3 μm), X-ray, mid-IR (3–30 μm), and the far-IR–radio ($>$ 30 μm); we do not consider the selection of obscured AGN at gamma-ray wavelengths since with current technology the majority of the gamma-ray detected AGN are highly beamed unobscured AGN (see Section 6 of Padovani et al. 2017 for a recent review). The selection of these wavebands correspond to those typically adopted in the literature and are mostly defined by the different technology required to observe in each waveband; however, we note that each waveband also broadly

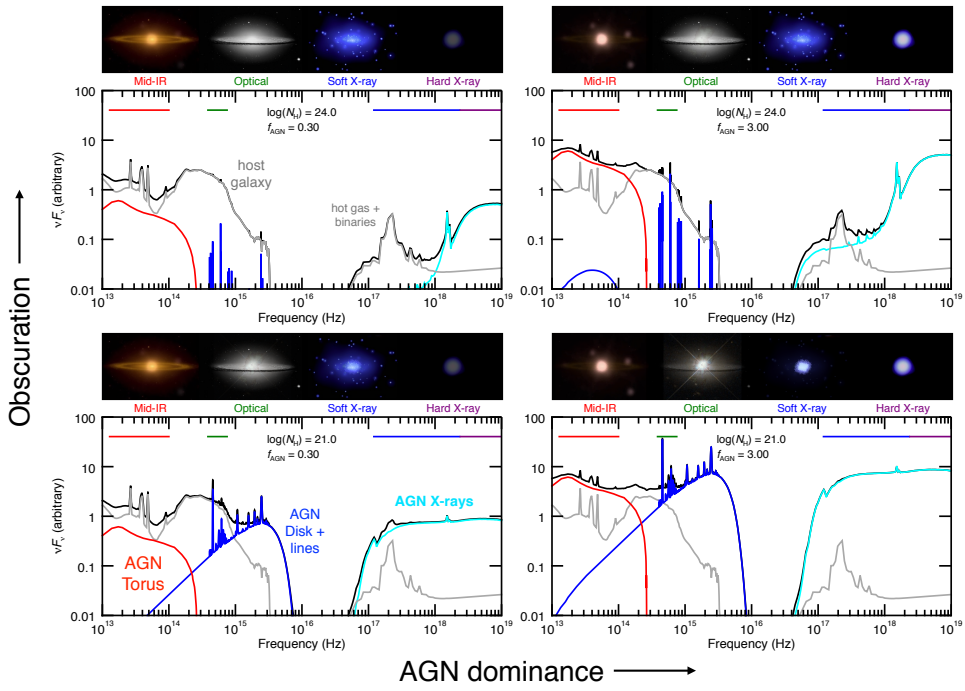

Figure 4

Schematic demonstrations of the multi-wavelength observational signatures of an AGN as a function of nuclear obscuration (increasing from bottom to top) and the relative luminosity of the AGN to the host galaxy (increasing from left to right). The nuclear obscuration is parameterised by $N_{\rm H}$ and the relative luminosity of the AGN to the host galaxy is based on the fraction of the intrinsic emission from the AGN at 1 μm ($f_{\rm AGN}$). The bottom component of each panel shows the overall model SED (red: AGN component; green: host-galaxy component; black: combination of AGN and host galaxy), indicating the emission from the host galaxy and the AGN. IR and optical spectral components are taken from Harrison (2014) and (Assef et al. 2010), optical AGN lines from Vanden Berk et al. (2001), and X-ray spectra from Revnivtsev et al. (2008) and Baloković et al. (2018). The top component of each panel indicates the broad features predicted to be observed in imaging data in the mid-IR, optical, and X-ray bands on the basis of the model SED, based on images of the galaxy M104 and quasar 3C 273 (images courtesy NASA).

corresponds to a specific physical component within the overall AGN SED (see **Figure 1**).

In each sub section we briefly describe the origin of the AGN emission in that waveband and discuss the impact that obscuration and host-galaxy dilution has on the identification of AGN activity. We then describe some of the common techniques adopted to identify AGN and qualitatively assess two key factors: the "reliability" and "completeness" of the technique. The "reliability" refers to how reliable a given technique selects an obscured AGN from other astrophysical source populations (i.e., how much the contamination from other source populations effect the selection of obscured AGN). The "completeness" refers to how complete the technique is in selecting obscured AGN (i.e., high completeness means that the technique is able to select nearly all obscured AGN). These two quantities are not necessarily correlated. A given technique may be able to select all obscured AGN

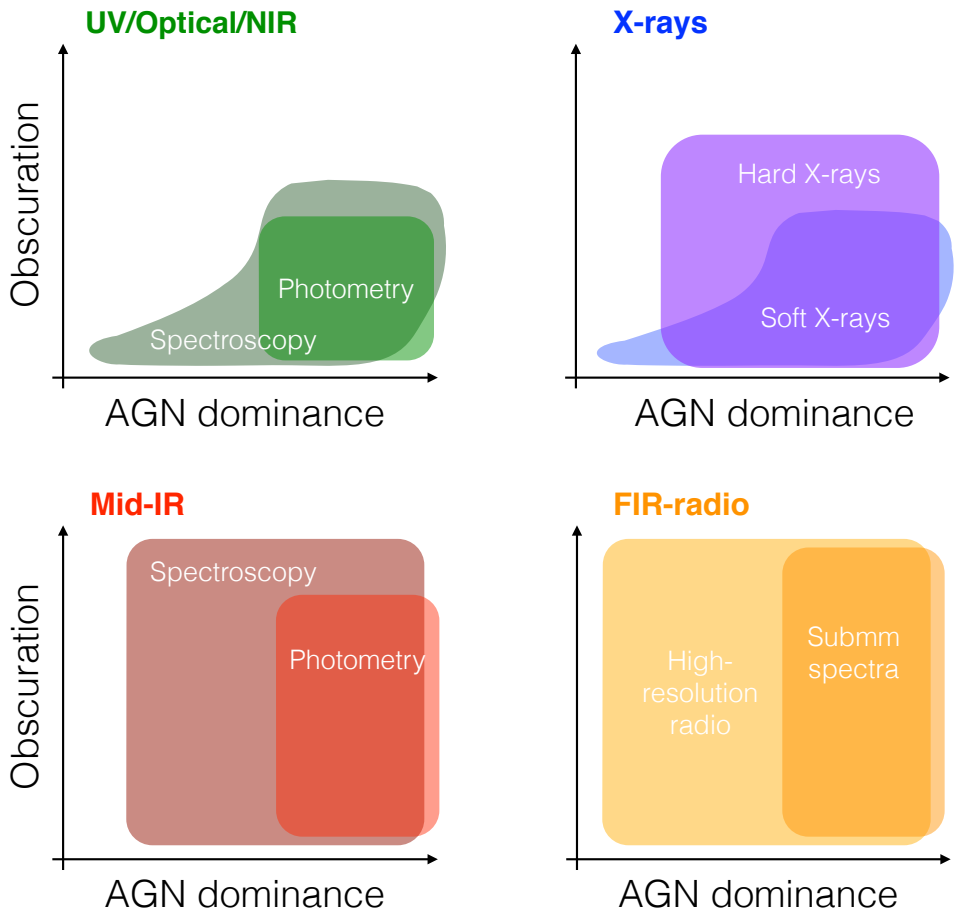

Figure 5

Schematic diagram to broadly illustrate the effectiveness of different techniques in the identification of AGN for a range in nuclear obscuration and the relative luminosity of the AGN to the host galaxy, as defined in **Figure 4**. The shaded regions indicate where the given technique is expected to be effective in identifying AGN activity within the obscuration–AGN dominance parameter space; despite the hard edges, these shaded regions should only be considered as broadly indicative.

but also be unreliable. An extreme example of this would be to select all galaxies in the Universe: this approach will select all obscured AGN, and so will have a high completeness; however, the majority of the selected sources will not host an obscured AGN and so the technique will have a low reliability. For the wavebands where both spectroscopy and broad-band photometry are adopted to select obscured AGN, we will discuss each separately. To provide some guidance in advance of our discussion, in **Figure 4** we illustrate the effects of obscuration on the broad-band AGN SED, and in **Figure 5** we schematically illustrate the impact that obscuration and host-galaxy dilution can have on the identification of AGN for a range of different techniques.

In our discussion we also indicate how accurately the amount of obscuration can be measured from a given technique. The best methods for identifying obscured AGN will typically not provide the most accurate measurements on the amount of obscuration because, by definition, they are relatively insensitive to the presence of obscuration (i.e., the optical depth is low and therefore the signatures of obscuration will not be strong).

We begin our discussion with UV–near-IR selection techniques, which were the first to identify obscured AGN, followed by a discussion of identification techniques at X-ray, mid-IR, and the far-IR–radio wavebands, highlighting the reliability and completeness of the various techniques for the selection of obscured AGN. This discussion builds on the recent review by Padovani et al. (2017), with a focus on obscured AGN. At the end of this section we discuss how a combination of techniques can be utilized to identify a more complete census of obscured AGN.

2.1. Selection of obscured AGN in the ultra-violet to near-infrared waveband

Some of the most well-developed selection techniques for obscured AGN are in the UV, optical, and near-IR wavebands. A summary of methods for identifying obscured AGN in these bands is given in the sidebar on "Common UV/optical/near-IR selection criteria for obscured AGN", and these are discussed in detail below.

2.1.1. Broad-band continuum techniques. Unobscured AGN are efficiently selected using UV–optical photometry since the emission from the accretion disk is bright in this waveband (e.g., Richards et al. 2001; Padovani et al. 2017); see **Figure 1**. However, UV–optical photometry is ineffective at identifying obscured AGN because (1) the optical depth due to dust is high at UV–optical wavelengths and hence the emission from the accretion disk is easily obscured (the optical depth increases towards shorter wavelengths; e.g., Calzetti, Kinney & Storchi-Bergmann 1994; Draine 2003b) and (2) the host galaxy is bright at UV–optical wavelengths due to the emission from stars, which dilutes the weak emission from the obscured AGN. As a consequence both the reliability and completeness of obscured AGN selection using UV–optical photometry is low.

Improvements in the selection of obscured AGN can be made by extending out to near-IR wavelengths as the optical depth is substantially lower than at UV–optical wavelengths. However, the stellar emission from galaxies typically peaks at near-IR wavelengths, offsetting part of the optical depth benefit. Consequently, the near-IR photometric selection of AGN is most effective for luminous AGN with modest amounts of obscuration, such as dust-reddened quasars where some of the accretion disk and broad-line emission is visible (e.g., Webster et al. 1995; Glikman et al. 2007); see Section 5.1 for further discussion.

The weakness of the AGN continuum of obscured AGN with respect to the host galaxy at UV–near-IR wavelengths does, however, make this waveband ideal for studying the host galaxies of obscured AGN (e.g., Kauffmann et al. 2003; Hickox et al. 2009; Schawinski et al. 2010; Heckman & Best 2014). Correspondingly, UV–optical emission that is faint and/or dominated by the host galaxy can be essential for classifying AGN as obscured when they are identified in other wavebands, as well as measuring the level of obscuration through fitting of the multiwavelength SED using empirical and/or theoretical models with varying levels of obscuration on the AGN component (e.g., Hickox et al. 2007; Merloni et al. 2014; see **Figure 3**).

2.1.2. Spectroscopic techniques. While UV–near-IR photometry is inefficient at identifying obscured AGN, UV–near-IR spectroscopy and spectropolarimetry have been essential tools in the identification and characterisation of obscured AGN. Optical spectroscopy led to the discovery of Seyfert galaxies (Seyfert 1943) and the identification of the two main spectral classes of AGN (e.g., Khachikian & Weedman 1974; Weedman 1977): Type 1 systems, where the bright optical continuum and both broad and narrow emission lines are observed (i.e., unobscured AGN), and Type 2 systems, where the optical continuum is weak and only narrow emission lines are observed (i.e., obscured AGN), as illustrated by the composite spectra shown in **Figure 3**. Optical spectropolarimety of Seyfert 2 galaxies has furthermore shown that many have the features expected for a Seyfert 1 galaxy (broad emission lines and a strong UV–optical continuum) when observed in polarized light (e.g., Antonucci & Miller 1985; Tran 2003; Moran et al. 2007; Ramos Almeida et al. 2016); this is commonly referred to as a "hidden Seyfert 1", a "hidden Type 1 AGN", or a "hidden BLR". The Seyfert 1 features are undetected in optical spectroscopy due to the obscuring torus but are seen in spectropolarimetry due to the emission being scattered (and hence polarized), by electrons/dust grains within the NLR, into the line of sight of the observer. Spectropolarimetry was central to the development of the unified AGN model and our current picture of the AGN physical structure.

A key reason why UV–near-IR spectroscopy has been so instrumental in the identification and characterization of obscured AGN is because the UV–near-IR waveband is rich in emission lines; some of the prominent optical lines are shown in **Figure 3**. From a combination of emission-line strengths it is possible to make sensitive measurements of the conditions of the different gas phases (e.g., from the excitation and ionization energies and critical densities), allowing for the construction of powerful emission-line diagnostic diagrams to distinguish obscured AGN from other astrophysical sources (e.g., Baldwin, Phillips & Terlevich 1981; Veilleux & Osterbrock 1987; Ho, Filippenko & Sargent 1997; Kewley et al. 2006). An example suite of emission-line diagnostic diagrams is shown in **Figure 6**. An AGN is distinguished from that of a star-forming region (i.e, HII region) and a LINER (low-ionization nuclear emission region sources, some of which host low-luminosity AGN; e.g., Heckman 1980; Heckman & Best 2014) on the basis of the ratio of the ionized forbidden line flux to the neutral permitted line flux: large ratios imply a "hotter" (i.e., shorter wavelength and higher energy) radiation field and betray the presence of the AGN. The emission-line ratios will be reduced if the AGN resides in a strong star-forming galaxy until, in extreme cases, the AGN signature is no longer distinguishable from that of star-forming galaxy. The emission lines are chosen to have similar wavelengths to reduce the effect of dust reddening on the emission-line ratio; however, the presence of obscuration will reduce the strength of the individual emission lines and could completely extinguish the emission-line signatures. For applications in which the available emission lines are limited due to the wavelength range of the spectra or the redshift of the source, complementary selection criteria have been developed that use a combination of line ratios and host galaxy properties such as color and mass (e.g., Trouille, Barger & Tremonti 2011; Yan et al. 2011; Juneau et al. 2011). Other studies have identified AGN by the presence of a single very high excitation optical line (commonly [NeV]λ3426) that is not easily excited by stellar processes (e.g., Gilli et al. 2010; Mignoli et al. 2013; Vergani et al. 2018).

Emission-line diagnostics provide a reliable method to identify AGN, although the demarcation curves between AGN and other source types depend on the metallicity of the systems and are expected to change with redshift (e.g., Kewley et al. 2013; Juneau et al.

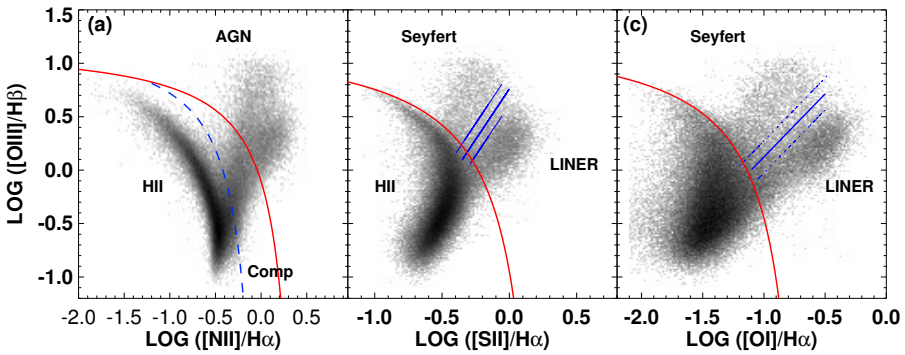

Figure 6

Optical emission-line diagnostic diagram to distinguish between AGN, star-forming galaxies (H II), composite AGN–star forming systems, and low ionisation nuclear emission region sources (LINERs). Figure from Kewley et al. (2006), courtesy of L. J. Kewley.

2014). They also provide a relatively complete selection of AGN and are able to identify systems with extreme nuclear obscuration since the NLR emission will not be heavily extinguished by obscuration of the nucleus on small scales (e.g., Zakamska et al. 2003; Lansbury et al. 2015; Hviding et al. 2018). However, the optical AGN signatures can be extinguished by dust in the host galaxy or rendered unidentifiable in systems where the host galaxy emission lines are significantly brighter than those of the AGN; the former limitation can be mitigated using spectroscopy at longer wavelengths (e.g., at mid-IR wavelengths), where the optical depth is lower; see Section 2.3.

The identification of a Type 2 AGN does not always indicate the presence of obscuration. At least a fraction of the Type 2 AGN population appear to be unobscured and intrinsically lack a BLR (e.g., Panessa & Bassani 2002; Bianchi et al. 2012). These systems often appear to be low-luminosity AGN and it is possible that the accretion rate is insufficient to allow for the formation of the optically thick accretion disk (e.g., Elitzur & Ho 2009; Trump et al. 2011); however, some high accretion rate systems also appear to intrinsically lack a BLR (e.g., Ho, Kim & Terashima 2012; Miniutti et al. 2013; Elitzur & Netzer 2016), challenging the simplest versions of the unified AGN model. The optical spectral properties of some AGN are also found to change from a Type 1 AGN to a Type 1.8–1.9 AGN (i.e., a system with with most of the features of a Type 2 AGN but with a weak broad-line component; Osterbrock 1981); these systems are often called "changing-look" AGN. For a fraction of these sources the changing optical spectral type may be related to changes in the obscuration properties (see Section 2.2 for X-ray evidence of time-variable absorption in AGN). However, in the majority of cases, it appears to be related to a decrease in the luminosity of the accretion disk (e.g., Denney et al. 2014; LaMassa et al. 2015; MacLeod et al. 2016).

UV–near-IR spectroscopy can provide reliable measurements of the amount of obscuration towards either the BLR or the NLR through the relative strength of related emission lines. The common adopted technique is called the "Balmer decrement" and is based on measuring the strength of the Hydrogen emission corresponding to different excitation states. For example, the Hα/Hβ flux ratio, which corresponds to the $n = 2$ (i.e., the

Balmer series) electron transitions, will have a fixed ratio for any given conditions of the gas (e.g., the density, metallicity, temperature; Baker & Menzel 1938; Brocklehurst 1971). Therefore, since optical depth is wavelength dependent, the presence of obscuring material will preferentially affect the Hβ emission (at 486 nm) more strongly than the Hα emission (at 656 nm), and therefore the deviation of the Hα/Hβ flux ratio from the expected flux ratio will indicate the amount of obscuration towards the line emitting regions (e.g., Ward et al. 1987; Gaskell 2017). The Balmer decrement is based on extinction measurements made from optical emission lines and is sensitive to modest amounts of obscuration; however, larger amounts of obscuration can be measured using longer-wavelength emission lines (e.g., the $n = 3$ Paschen series, which are produced in the near-IR waveband).

2.2. Selection of obscured AGN in the X-ray waveband

X-ray observations provide one of the most reliable and complete methods for selecting obscured AGN. A summary of X-ray methods for identifying obscured AGN is given in the sidebar on "Common X-ray selection criteria for obscured AGN", and we discuss them in detail below. The X-ray band is defined here as the energy range of 0.2–200 keV; energies below this range correspond to UV wavelengths and energies above this range correspond to gamma rays. The Earth's atmosphere is opaque at X-ray energies and therefore all sensitive X-ray observations of the cosmos have been obtained from space (see Giacconi 2009 for a review of the history of X-ray astronomy). It is common practice to divide the X-ray energy band into the "soft band" and "hard band", which corresponds broadly to the sensitivity of the X-ray observatory to the absorbing column density of gas. Although the definition of these bands can vary from study to study, in this review we will define the soft band as < 10 keV and the hard band as > 10 keV; on the basis of this definition, some of the current soft-band observatories are *Chandra* and *XMM-Newton* while some of the current hard-band observatories are *Integral*, *NuSTAR*, and *Swift*-BAT. The majority of X-ray observatories have good energy resolution and low background, allowing for simultaneous photometric and spectroscopic measurements from individual observations. Hence in this sub section we do not make a strong distinction between the photometric and spectroscopic identification of AGN.

The X-ray emission from AGN appears to be (near) ubiqitious and is directly associated with the accretion disk. In unobscured AGN there is a remarkably tight relationship between the X-ray emission and the UV–optical emission (e.g., Steffen et al. 2006; Lusso & Risaliti 2016). The X-ray emission is thought to arise in a "corona" above the accretion disk and is predominantly produced by the inverse Compton scattering of photons from the accretion disk; however, the lowest energy X-ray photons can be produced in the inner, and therefore hottest, regions of the accretion disk. The X-ray emission is then modified from interactions with material in the accretion disk (and potentially the host galaxy), such as photoelectric absorption, reflection, and scattering (see **Figure 1**).

The impact of obscuration in the X-ray band is a function of rest-frame energy, with lower-energy X-ray photons more easily absorbed than higher-energy X-ray photons (i.e., the optical depth increases with decreasing energy; Wilms, Allen & McCray 2000). As a consequence, observatories with sensitivity in the hard band are able to detect more heavily obscured AGN than observatories with sensitivity in the soft band; however, we note that it depends on the redshift of the source since the probed rest-frame energy increases with redshift in a given energy band. The low optical depth at X-ray energies, particularly in

the hard band, means that the completeness of obscured AGN selection is high in the X-ray waveband. For example, at X-ray energies of > 10 keV significant suppression of the X-ray emission only occurs at Compton-thick column densities ($N_{\rm H} > 1.5 \times 10^{24}$ cm^{-2}) due to Compton recoil and subsequent absorption of the X-ray photons (see Comastri 2004 for a review).

X-ray observations also provide one of the most reliable methods to identify AGN because the X-ray emission from other astrophysical processes is typically weak by comparison. The dominant physical processes for the production of X-ray emission in the host galaxy are accreting neutron stars and stellar-mass black holes (commonly referred to as X-ray binaries; see Fabbiano 2006 for a review) and hot gas ($T > 10^6$ K). The populations of X-ray binaries are classified into low-mass X-ray binaries and high-mass X-ray binaries, depending on the mass of the stellar companion in the binary system, and their integrated X-ray luminosities are closely related to the mass and star-formation rate of the galaxy, respectively (e.g., Lehmer et al. 2016). Only the most massive and strongly star-forming galaxies will produce X-ray emission of $L_{\rm X} > 10^{42}$ erg s^{-1} at 2–10 keV (e.g., Alexander et al. 2005; Wang et al. 2013) and the majority of galaxies will be more than an order of magnitude less luminous in the X-ray band (e.g., Lehmer et al. 2010; Mineo, Gilfanov & Sunyaev 2012). Therefore, contamination from host-galaxy processes is only likely to be an issue for low luminosity or heavily obscured AGN, where the X-ray emission is suppressed due to the presence of absorption. For nearby systems, such weak or obscured AGN may be identified using high-resolution X-ray observations if an X-ray point source can reliably associated with the galactic nucleus (e.g., Gallo et al. 2010; She, Ho & Feng 2017). However, we caution that there can still be a non-negligible chance that a nuclear X-ray source is an X-ray binary rather than an AGN, highlighting the importance of additional discriminating criteria such as those described in this review.

Since the integrated emission from X-ray binaries is predominantly observed at $<$ 10 keV, low luminosity or heavily obscured AGN can be more reliably identified at > 10 keV. The emission from hot gas, either from the host galaxy or from a galaxy cluster, can be substantial in some sources (up-to $\approx 10^{41}$–10^{42} erg s^{-1} for AGN in luminous host galaxies and up-to $\approx 10^{44}$–10^{45} erg s^{-1} for AGN that reside at the core of a massive galaxy cluster); however, as for the X-ray binaries, the X-ray emission from the hot gas is predominantly at low energies ($<$ 2–5 keV). Overall, the combination of the low optical depth and the low contrast between AGN and other astrophysical source populations at X-ray energies, particularly in the hard band, make X-ray observations one of the most reliable and complete methods to select obscured AGN (Brandt & Alexander 2015).

The distinctive signatures of absorption in the X-ray spectra of AGN (illustrated in **Figure 4**) mean that X-ray spectroscopy provides one of the most accurate methods of identifying obscuration in AGN and measuring the amount of absorption, at least up to Compton-thin absorbing column densities (e.g., Done 2010). For sources with relatively few detected X-ray counts, the level of absorption can be approximated using the hardness ratio (the ratio of source counts in different X-ray bands; Park et al. 2006) and source redshift (e.g., Merloni et al. 2014).

The signatures of Compton-thick absorption are more challenging to detect, but can be identified in high signal-to-noise ratio X-ray spectra. The identification of a strong reflection component at $E > 10$ keV and a prominent Fe Kα emission line at 6.4 keV (with equivalent width typically $>$1 keV) are clear signatures of Compton-thick absorption (e.g., Mushotzky, Done & Pounds 1993; Levenson et al. 2006; Done 2010). The presence of Compton-thick

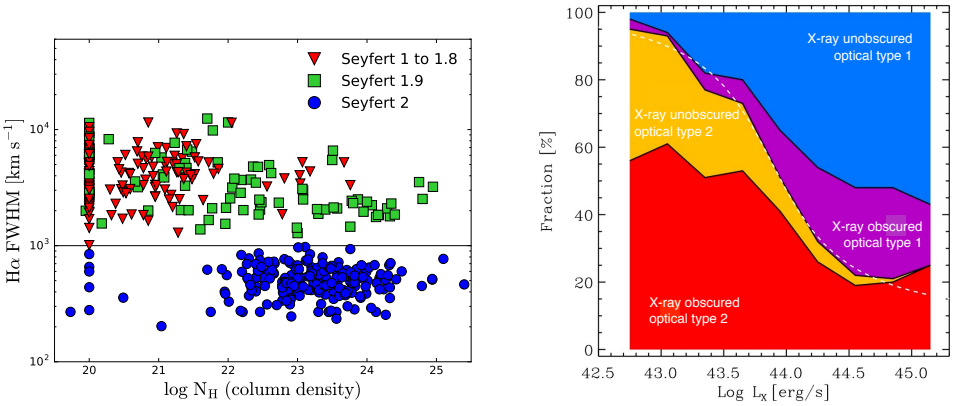

Figure 7

(Left) *Hα* emission-line width (parameterised as the full width half maximum) vs absorbing column densities for local X-ray AGN detected by *Swift*-BAT. The symbols indicate the different optical spectral types of the X-ray AGN and the solid horizontal line indicates the broad separation between Type 1 and Type 2 AGN in this study. Figure from Koss et al. (2017), courtesy of M. Koss. (Right) Relative fractions of AGN vs X-ray luminosity for the broad redshift range of $z = 0.3$–3.5. The relative fractions are distinguished according to their X-ray and optical classifications. Figure modified from Merloni et al. (2014), courtesy of A. Merloni.

material can also be inferred through the comparison of the observed X-ray luminosity to a proxy (such as mid-IR or optical narrow-line emission) for the intrinsic X-ray luminosity, although this is a less reliable approach; see Section 2.5. On the basis of current constraints, the fraction of the AGN population that is Compton thick is high (≈ 30–50%; e.g., Burlon et al. 2011; Ricci et al. 2015); see Section 3.

The source of the obscuration at X-ray energies (gas) is different to the source of the obscuration at longer wavelengths (dust) and may occur on different physical size scales. Despite this, good agreement is found between the X-ray signatures of absorption and the optical spectral types of AGN if $N_{\rm H} = 10^{22}$ cm^{-2} is taken as the threshold between X-ray absorbed and X-ray unabsorbed AGN (≈ 80–90% agreement in the X-ray and optical obscuration signatures; e.g., Malizia et al. 2012; Merloni et al. 2014; Burtscher et al. 2016; Koss et al. 2017); see **Figure 7**.

The X-ray absorption in the majority of AGN is not constant but is seen to vary on time scales of days to years (e.g., Risaliti, Elvis & Nicastro 2002; Bianchi et al. 2009), indicating that the absorbing gas is distributed in compact clouds; individual AGN have even been seen to change from Compton thin to Compton thick levels of absorption and vice versa (e.g., Matt, Guainazzi & Maiolino 2003; Risaliti et al. 2005). Current constraints suggest that much of the variable absorption of the X-ray emission occurs in the BLR rather than in the dusty torus.

2.3. Selection of obscured AGN in the mid-infrared waveband

The mid-IR waveband provides an efficient and effective selection of obscured AGN. A summary of mid-IR methods for identifying obscured AGN is given in the sidebar on "Common mid-IR selection criteria for obscured AGN", and we discuss them in detail below. The mid-IR waveband is defined here as 3–30 μm, which broadly corresponds to the infrared

wavelengths where the emission from the AGN is most distinct from that of the host galaxy; see **Figure 1**. Due to strong absorption in the terrestrial atmosphere, the majority of the mid-IR waveband can only be efficiently observed from high in the atmosphere and, ideally, from space; some of the observatories with sensitivity at mid-IR wavelengths, from the past and present, are *Akari*, *IRAS*, *ISO*, *SOFIA*, *Spitzer*, and *WISE* (see Lutz 2014, for a review). There are several narrow wavebands where the mid-IR emission can penetrate through the atmosphere and be detected using ground-based telescopes. However, the sensitivity of ground-based telescopes to the detection of mid-IR emission is low when compared to those from space since the mid-IR waveband corresponds to thermal emission at $\approx$ 100–1000 K and therefore any "hot" objects (including astronomers!) are a significant source of background noise; by comparison, space-based observatories can be efficiently cooled, reducing the thermal background noise. However, ground-based telescopes often have significantly larger mirrors than the space-based telescopes, allowing for higher-resolution imaging.

2.3.1. Broad-band continuum techniques. AGN are bright in the mid-IR waveband due to the thermal emission from warm–hot dust in the torus, which is heated by the absorption of shorter-wavelength photons from the accretion disk. The strength of the mid-IR emission from the AGN depends on the covering factor of the dust around the accretion disk (i.e., the fraction of the photons from the accretion disk that are absorbed by the dust); see Section 4.1. The optical depth is low at mid-IR wavelengths and therefore, unlike the UV–near-IR waveband, the emission is not strongly suppressed by the obscuring dust. Consequently, the completeness of the selection of obscured AGN at mid-IR wavelengths can be high, although see some of the caveats noted below. However, other astrophysical sources also produce strong infrared emission, most notably dust-obscured star formation from the host galaxy, which effects the overall reliability of AGN selection in the mid-IR waveband, particularly for lower-luminosity systems where the emission from the AGN can be weak compared to that of the host galaxy. Fortunately, the SEDs of AGN and star-forming galaxies significantly differ (e.g., star-forming galaxies have "cooler" SEDs; see **Figure 1**), at least for the majority of objects, and hence a variety of techniques can be employed to identify AGN from star-forming galaxies.

A common approach adopted to identify AGN at mid-IR wavelengths is to use color-color diagnostics; see Table 2 of Padovani et al. (2017) for a comprehensive list of different infrared color-color diagnostics. The basic principle behind this approach is the same as that adopted for unobscured AGN searches using UV–optical color-color diagnostics; i.e., exploiting differences between the SEDs of AGN from other astrophysical source populations. However, the key advantage that the mid-IR waveband provides over the UV–optical waveband is that both obscured and unobscured AGN are selected. The first color-color diagnostics in the infrared waveband were developed over 30 years ago using broad-band data over 12–100 μm from the *IRAS* observatory (e.g., de Grijp et al. 1985; Low et al. 1988). More recently, mid-IR color-color diagnostic diagrams have been developed based around the sensitive *Spitzer* and *WISE* observatories at 3–24 μm (e.g., Stern et al. 2005; Alonso-Herrero et al. 2006; Mateos et al. 2012; Assef et al. 2013). Although powerful, these color-color diagnostics do have some limitations: (1) the source needs to have a strong AGN component to be selected and hence systems with weak AGN components (e.g., intrinsically weak AGN or AGN hosted in strongly star-forming galaxies) are not easily identified and (2) the mid-IR colors of high-redshift ($z > 2$–3) star-forming galaxies can be similar to those of AGN and hence "contaminate" the AGN selection parameter space in the color-color

diagrams. These limitations can be mitigated to a large extent by further requiring a minimum flux threshold (which removes the high-redshift star-forming galaxies, which are faint at mid-IR wavelengths) or by combining mid-IR data with far-IR data to construct broad-band infrared SEDs to search for weaker AGN components in the mid-IR waveband (see Section 2.4). In nearby systems, high spatial resolution mid-IR observations can distinguish a compact nucleus from more extended star formation and so potentially identify weaker AGN (e.g., Siebenmorgen et al. 2008). Overall, the completeness of the AGN selection in the mid-IR waveband can be high, but the reliability of the AGN selection is modest and depends on how the aforementioned caveats are handled.

A surprising result from the analysis of the mid-IR continuum of AGN is that obscured AGN have broadly similar mid-IR SEDs to unobscured AGN, both when using measurements on the scale of the whole galaxy (e.g., Buchanan et al. 2006; Mateos et al. 2012; Hickox et al. 2017; see **Figure 3**) and for spatially-resolved measurements on ∼pc scales (e.g. Ramos Almeida et al. 2011; Asmus et al. 2014). This is in disagreement with that expected from the basic unified AGN model, since the presence of obscuration should suppress the mid-IR emission from an obscured AGN (with greater suppression of the shorter-wavelength emission). Indeed, it is often not possible to reliably distinguish between an obscured and unobscured AGN on the basis of just the mid-IR colors, and optical or X-ray data are required to determine whether the AGN is obscured or unobscured (e.g., Barmby et al. 2006; Hickox et al. 2007). These findings are a key driver behind the idea that the obscuring dust in AGN is not distributed in a smooth torus but is clumpy and allows for the mid-IR emission to escape from the torus without being obscured (e.g., Netzer 2015; Ramos Almeida & Ricci 2017); see Section 4.1. Furthermore, high spatial resolution mid-IR imaging has also revealed that a large fraction of the mid-IR emission from some obscured AGN is produced from dust in the polar regions rather than the torus (e.g., Raban et al. 2009; Asmus, Hönig & Gandhi 2016; see **Figure 2** and Section 4.1.5).

2.3.2. Spectroscopic techniques. Strong discrimination between AGN and star-forming galaxies can be achieved using mid-IR spectroscopy. The "hotter" radiation field from the accretion disk, when compared to that from star-forming regions, means that the detection of high excitation emission lines (e.g., [Ne VI] 7.6 μm; [Ne V] 14.3 μm; see Spinoglio & Malkan 1992) provides an almost unambiguous identification of AGN activity. However, the equivalent width of these high-excitation emission lines is often low when compared to emission lines at UV–optical wavelengths, making them sometimes challenging to detect. Despite this, the low optical depth at mid-IR wavelengths (e.g., Draine 2003b) facilitates the detection of emission lines in heavily dust-obscured regions where the UV–optical signatures of AGN activity are extinguished (e.g., Satyapal et al. 2008; Goulding & Alexander 2009; Pereira-Santaella et al. 2010). Overall, this technique provides an obscured AGN identification approach with high completeness and reliability; however, the lack of large-scale mid-IR spectroscopic facilities mean that the sample sizes are currently small when compared to those available from UV–optical spectroscopy.

The mid-IR spectra of AGN and star-forming galaxies also differ in the strength of the broad-band spectral features due to polycyclic aromatic hydrocarbon (PAH) molecules (e.g., Tielens 2008). PAHs appear to be ubiquitous in the interstellar medium of galaxies (e.g., Peeters, Spoon & Tielens 2004; Smith et al. 2007) and are broadly correlated with the star-formation component of galaxies. As a consequence, the equivalent width of the PAH features can be used to assess the relative strength or weakness of emission from the AGN

in the mid-IR waveband. An advantage of this approach is that lower resolution mid-IR spectroscopy can be employed than that required for the detection of emission lines since the PAH features have large equivalent widths (e.g., Genzel et al. 1998; Pope et al. 2008). Weak AGN components can be identified with this approach and it is particularly effective when combined with mid-IR–far-IR photometry to provide a broader wavelength baseline to constrain the strength of both the AGN and star-formation components; see Section 2.4.

Mid-IR spectroscopy can provide a reliable route to measure the amount of obscuration towards the AGN. The primary spectroscopic diagnostic is a strong absorption feature due to Si-based dust grains at 9.7 and 18 μm (e.g., Draine & Lee 1984). The depth of the Si absorption feature provides an estimate on the amount of obscuration towards the mid-IR emitting region of the AGN. Obscured AGN are often found to have Si absorption features while unobscured AGN typically have Si emission features (e.g., Hao et al. 2007; Hatziminaoglou et al. 2015; Alonso-Herrero et al. 2016a). Overall a broad correlation is found between the strength of the Si absorption and the absorbing column density measured using X-ray data (e.g., Shi et al. 2006; Hönig et al. 2010). The presence of strong Si absorption is therefore sometimes taken as an indicator for a obscured AGN, revealing potentially extremely obscured AGN that lack AGN signatures at other wavelengths (e.g., Imanishi et al. 2007; Georgantopoulos et al. 2011). However, not all obscured AGN have strong Si absorption, including perhaps half of the Compton-thick AGN population, and the origin of the Si absorption feature often appears to be due to dust in the host galaxy rather than the torus (e.g., Goulding et al. 2012).

2.4. Selection of obscured AGN at far-infrared–radio wavelengths

AGN produce emission across a broad range of wavelengths and therefore obscured AGN can be selected at wavebands not explored so far in this review; see **Figure 1**. The far-IR–radio waveband, in particular, provides the potential for many significant advances over the selection of obscured AGN at other wavelengths, principally because the optical depth is very low at these wavelengths (Hildebrand 1983), allowing for even the most heavily obscured AGN missed in the X-ray and mid-IR wavebands to be selected. However, the full potential of these wavebands for the selection of obscured AGN is yet to be realised due to the relatively modest sensitivities of current facilities. A summary of far-IR–radio methods for identifying obscured AGN is given in the sidebar on "Common far-IR–radio selection criteria for obscured AGN", and we discuss them in detail below.

2.4.1. Far-infrared–millimeter wavelengths. The continuum emission at far-IR–millimeter wavelengths (30 μm–10 mm) from the majority of AGN is dominated by dust heated from star formation in the host galaxy. This limits the effectiveness of AGN identification on the basis of far-IR–millimeter photometry alone. However, when the mid-IR photometry is combined with the far-IR–millimeter photometry to construct the broad-band IR–millimeter SED, the signature of an AGN component can be identified through fitting the SED with AGN and star-forming galaxy templates or models. This approach can potentially identify weaker AGN components than that achieved through mid-IR photometry alone (e.g., Pope et al. 2008; Sajina et al. 2012; Del Moro et al. 2016) and is particularly effective when combined with mid-IR spectroscopy (see Section 2.3.2).

Obscured AGN can also be identified using dense molecular gas tracers with (sub)-millimeter spectroscopy (e.g., HCN and HCO+; Gao & Solomon 2004; Aalto et al. 2015;

Imanishi, Nakanishi & Izumi 2016). These emission lines from dense molecular gas are radiatively excited by mid-IR photons and can therefore reveal the presence of an obscured AGN. A similar technique uses observations of CO lines, for which the relative strengths of the rotational transitions depend on the excitation mechanism, and a high ratio of high-excitation to low-excitation CO lines can indicate heating from an AGN (e.g., Rosenberg et al. 2015; Mingozzi et al. 2018). Since the optical depth is very low even for Compton-thick levels of absorption at (sub)-millimeter wavelengths (Hildebrand 1983), heavily obscured AGN missed at other wavelengths can be identified using (sub)-millimeter spectroscopy (e.g., Aalto et al. 2015; Imanishi, Nakanishi & Izumi 2016); however, dilution from star formation within the host galaxy will weaken the AGN signature. This approach offers great potential to extend our census of obscured AGN, although given the sensitivity of current facilities, the majority of obscured AGN searches with this technique are limited to comparatively nearby systems.

2.4.2. Radio wavelengths. The identification of AGN in the radio waveband ($\approx$ 0.01–30 m) has a long history going back to the first detected quasars (e.g., Baade & Minkowski 1954; Schmidt 1963). The dominant physical process for AGN in the radio waveband is synchrotron emission, which can be due to processes related to the accretion disk and/or large-scale radio jets (see Padovani 2016; Tadhunter 2016 for a recent review). The optical depth for radio emission is very low and so radio selection can identify very heavily obscured sources (e.g., Wilkes et al. 2013), although synchrotron self absorption can occur in compact radio-emitting sources and H I absorption is seen at 21 cm (the spin-flip transition). However, AGN are not the only extragalactic source population that can produce significant radio emission: star-forming galaxies can also be bright in the radio band (e.g., Condon 1992).

At the highest radio luminosities (e.g., $> 10^{25}$ W Hz^{-1} at 1.4 GHz) AGN are uniquely distinguished from star-forming galaxies: these sources are often referred to as "radio-loud" AGN and comprise a minority of the overall AGN population, which is predominantly radio quiet (e.g., Padovani 2016; Tadhunter 2016). At lower radio luminosities AGN cannot be reliably distinguished from star-forming galaxies on the basis of luminosity alone. However, since the radio luminosity from star formation is tightly correlated with the far-IR luminosity (e.g., Helou, Soifer & Rowan-Robinson 1985; Condon 1992), AGN can be identified by selecting sources that produce excess radio emission over that expected from star formation (e.g., Donley et al. 2005; Del Moro et al. 2013). When multi-frequency radio data are available, the radio spectral slope can also be used to identify AGN activity: a flat radio spectral slope ($\alpha < 0.5$; e.g., Padovani 2016) indicates a compact source (synchrotron self absorbed) and therefore an AGN with a steep radio spectral slope can be due to either AGN activity or star formation. Higher spatial resolution data (e.g., very long baseline interferometry data) can also be used to identify the presence of AGN activity over star formation: an unresolved radio core, radio jets, and radio lobes indicate the presence of an AGN (e.g., Padovani 2016; Tadhunter 2016). Radio wavelengths can therefore provide reliable obscured AGN selection with high completeness, particularly at high radio luminosities. However, the reliability of the obscured AGN selection in the radio band decreases towards lower luminosities and depends on the luminosity of the radio core and the multi-wavelength data available.

The radio waveband can also provide reliable absorption measurements. The identification of the neutral H I absorption feature at 21 cm provides a measurement of the H I

column density towards the radio-emitting source. Current studies suggest a connection between the neutral H I absorbing column at 21 cm with the absorbing columns measured in the X-ray band (e.g., Ostorero et al. 2016; Moss et al. 2017); however, the current sample sizes are small and greater progress will be made with future radio facilities such as the Square Kilometer Array (SKA); see Section 6.1.5.

2.5. Multi-wavelength identification and a comparison of selection methods

No single waveband provides a complete and reliable selection of AGN with current facilities. The low optical depth at mid-IR–radio wavelengths ensures weak obscuration effects and hence high obscured-AGN completeness, although contamination of the AGN emission from the host galaxy reduces the reliability of the AGN selection when the host galaxy is bright with respect to the AGN. The reliability of the AGN selection at mid-IR–radio wavelengths can be significantly improved with high spatial resolution observations, where the relative contrast between the AGN and the galaxy will be higher, and from spectroscopic observations, where the identification of emission lines and solid-state features provide constraints on the relative strength of the AGN and host-galaxy emission processes. However, the availability of high spatial resolution and spectroscopic observations at mid-IR–radio wavelengths is limited when compared to broad-band photometric data. By comparison, UV–optical spectroscopy is often more readily available (thanks to ground-based multi-object spectrographic instruments) and can select AGN with good reliability and completeness but is biased against identifying AGN that reside in galaxies that are either strongly dust obscured or bright when compared to the AGN. The X-ray waveband has low optical depth, particularly in the hard band, and the host-galaxy contamination is low, allowing for the reliable selection of obscured AGN except for low-luminosity systems; however, Compton-thick AGN are weak and can be challenging to identify at X-ray energies.

Due to the limitations in the identification of obscured AGN in any given waveband, a more complete selection will be achieved from a combination of multi-wavelength identification approaches. For example, an AGN selection approach that combines X-ray, infrared, and radio data (e.g., such as that available for many of the blank-field extragalactic survey areas) will reduce the identification biases of any individual waveband. Such an approach would allow for the identification of X-ray detected Compton-thin AGN even in strongly star forming galaxies, the identification of potential infrared-bright Compton-thick AGN from the weak or non detection of X-ray emission, and the identification of radio-bright AGN that are heavily obscured in both the X-ray and infrared wavebands (e.g., Hickox et al. 2009; Del Moro et al. 2013, 2016). In **Figure 8** we demonstrate the complementarity of infrared and X-ray data in identifying potential Compton-thick AGN from the detection of bright mid-IR emission from the AGN with weak or undetected X-ray emission (e.g., Alexander et al. 2008; Vignali et al. 2010; Lansbury et al. 2015, 2017). Combining these multi-wavelength data with spectroscopic observations would provide an even more complete selection of obscured AGN.

However, despite the obvious advantage of a multi-wavelength approach in terms of providing a more complete selection of AGN, the relative simplicity of the single waveband approach does have a key attribute: a simple selection function. The selection function is the quantification of the sensitivity and identification biases and will be much simpler for a single waveband approach than for a multi-wavelength approach. Therefore, if the effect of obscuration and host-galaxy dilution is well understood in the selected waveband then it

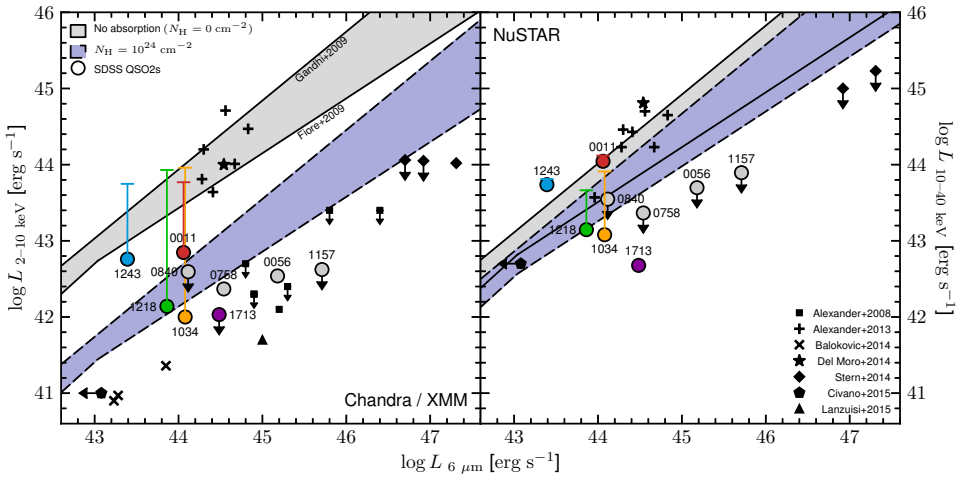

Figure 8

X-ray luminosity versus 6 μm AGN luminosity for AGN explored in a variety of studies using (left) *Chandra* or *XMM-Newton* soft-band (2–10 keV) constraints and (right) *NuSTAR* hard-band (10–40 keV) constraints. The symbols indicate the observed X-ray luminosities and the solid vertical lines indicate the intrinsic (i.e., corrected for absorption) X-ray luminosities for the sources with absorbing-column measurements. The grey shaded region indicates the range in intrinsic X-ray–6 μm AGN luminosity relationships between Fiore et al. (2009) and Gandhi et al. (2009) and the blue shaded region indicates the same relationships but where the X-ray luminosity is absorbed by a column density of $N_H = 10^{24}$ cm^{-2}. Taken from Lansbury et al. (2015), courtesy of G. Lansbury.

can be used to *model* the data and *infer* the properties of the overall AGN population (i.e., taking into account the AGN not selected due to sensitivity and identification biases). We have emphasized *model* and *infer* here since this approach is model based (e.g., it makes assumptions about the AGN and host galaxy properties, an example being the distribution of AGN absorbing column densities) and the complete AGN population is inferred rather than directly identified. For complex selection functions that depend on several variables, an effective technique is to simulate the overall AGN population and then apply the same identification procedure to the simulated data; this technique is commonly referred to as "forward modeling"; see Section 6.2. The selection function is then the difference between the input and the output (i.e., the overall AGN population and the subset of the AGN population that are identified).

Multi-wavelength and single-waveband identification approaches are therefore complementary. The multi-wavelength approach can construct a (near) complete census of AGN in, for example, a given volume down to a given luminosity. It requires more extensive data than the single-waveband approach and will likely be limited in the volume–luminosity parameter space that it can cover. However, the knowledge of the AGN properties gained from this approach can then guide the modeling required to infer the overall AGN population from a single waveband approach, which requires less extensive multi-wavelength data and can extend over larger regions of parameter space. One application of this approach is constraining the properties of the Compton-thick AGN population. X-ray data are essential in identifying Compton-thick AGN as it is required to constrain the absorbing column density.

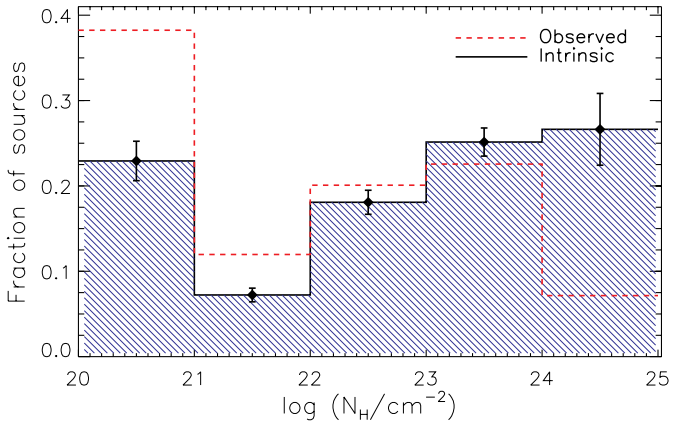

Figure 9

Distribution of absorbing column densities ($N_{\rm H}$ distribution) for local AGN from the *Swift*-BAT survey. Both the observed distribution (red dashed line) and the intrinsic distribution (black solid line) are shown. A comparison between the two distributions demonstrate the large corrections required to determine the intrinsic fraction of Compton-thick AGN with $N_{\rm H} = 10^{24}$–10^{25} cm^{-2}. Taken from Ricci et al. (2017), courtesy of C. Ricci.

However, a flux-limited X-ray survey is biased against detecting Compton-thick AGN due to the suppression of the X-ray emission and, therefore, significant corrections are required to infer the overall Compton-thick AGN population (e.g., an observed fraction of $\approx 8^{+1}_{-2}\%$ vs an intrinsic fraction of $\approx 27 \pm 4\%$ from the hard-band selected *Swift*-BAT survey; Ricci et al. 2015; see **Figure 9**). The multi-wavelength identification and characterisation of all AGN, including measuring (or inferring) the absorbing column densities, within a given volume (e.g., Goulding & Alexander 2009; Annuar et al. 2015, 2017) is therefore essential to validate the modeling assumptions adopted in the single waveband approach. Furthermore, since all of the AGN are identified and characterised in the volume-limited study, it will include systems that have abnormal properties or are intrinsically weak in any given waveband, extending our understanding of the overall AGN population.

3. The Demographics of the Obscured AGN population

As a prelude to the next section on the physical nature of obscuration in AGN we provide a brief overview of the observed demographics of obscured AGN activity. In this section we discuss three key aspects: (1) the distribution of AGN absorbing column densities, including the fraction of AGN that are Compton thick, (2) the luminosity dependence of obscuration, and (3) the redshift dependence of obscuration. We will mostly focus our discussion on results from X-ray observations since they provide an efficient AGN selection and yield one of the most reliable absorption measurements; however, we will note similarities and discrepancies with results obtained at other wavelengths.

The majority of the AGN population are obscured: they dominate both the number density and luminosity density of accretion onto SMBHs (e.g., Ueda et al. 2014; Aird et al. 2015b; Buchner et al. 2015). A common way to characterise the amount of obscuration is to construct the distribution of absorbing column densities (often called the $N_{\rm H}$ distribution).

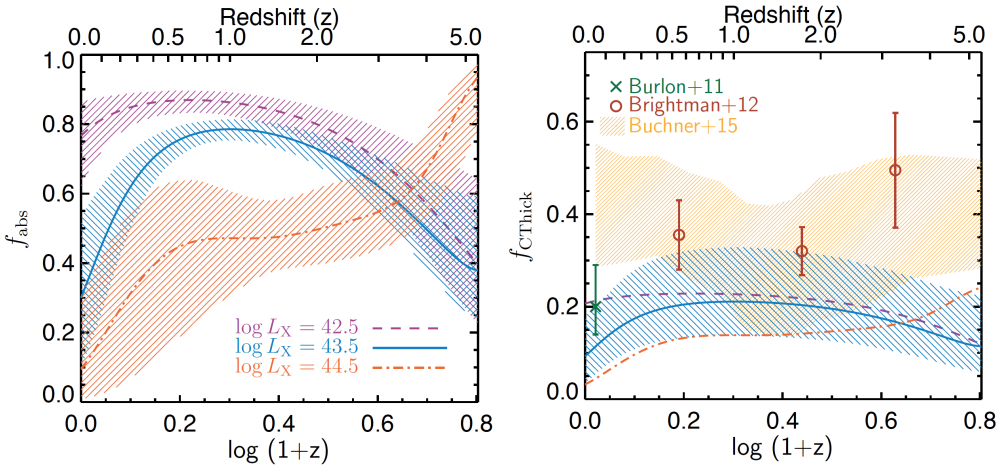

Figure 10

(Left) Fraction of AGN that are X-ray absorbed but Compton thin vs redshift for three different rest-frame 2–10 keV luminosities (colored coded, as indicated) for the best-fitting model presented in Aird et al. (2015b). (Right) Fraction of AGN that are Compton-thick vs redshift at a rest-frame 2–10 keV luminosity of $10^{43.5}$ erg s^{-1} (blue curve and shaded region), compared to other studies (as indicated) for the best-fitting model presented in Aird et al. (2015b). The magenta and orange curves show the Compton-thick AGN fraction vs redshift at a rest-frame 2–10 keV luminosity of $10^{42.5}$ erg s^{-1} and $10^{44.5}$ erg s^{-1}, respectively. Figures taken from Aird et al. (2015b), courtesy of J. Aird.

In **Figure 9** we show an example $N_{\rm H}$ distribution for AGN in the local Universe detected at 14–195 keV from the *Swift*-BAT all-sky survey (Ricci et al. 2017b). The absorbing column densities have been measured using the *Swift*-BAT data in combination with X-ray data in the soft band and both the observed and *intrinsic* (i.e., the inferred $N_{\rm H}$ distribution after correcting for the selection function; see Section 2.5) distributions are plotted. The intrinsic fraction of obscured AGN ($N_{\rm H} > 10^{22}$ cm^{-2}) from this study is $70 \pm 5\%$ and the intrinsic fraction of Compton-thick AGN ($N_{\rm H} = 10^{24}$–10^{25} cm^{-2}) is $27 \pm 4\%$ (e.g., also see Akylas et al. 2016; Koss et al. 2016). Note that the absence of heavily Compton-thick AGN with $N_{\rm H} > 10^{25}$ cm^{-2} is not intrinsic but is due to the low sensitivity of X-ray observations to such large amounts of obscuration and therefore the Compton-thick fraction is actually a lower limit. An effective technique that can be adopted to identify heavily Compton-thick AGN is to combine mid-IR and X-ray observations to select AGN that are bright in the mid-IR waveband but weak or undetected at X-ray energies; see Section 2.5 and **Figure 8**.

The fraction of AGN that are obscured appears to be a function of both AGN luminosity and redshift. The first tentative evidence of this result was found over 25 years ago (Lawrence 1991) and has since been confirmed by many studies in the X-ray, optical, infrared, and radio wavebands (e.g., Simpson 2005; Maiolino et al. 2007; Treister, Krolik & Dullemond 2008; Lusso et al. 2013; Mateos et al. 2017). An example of the obscuration dependence with AGN luminosity is shown in **Figure 7** for X-ray detected AGN over the broad redshift range of $z = 0.3$–3.5 (Merloni et al. 2014). An interesting attribute of this chosen example is that the distinction between obscured and unobscured AGN is made using both X-ray data and optical spectroscopy. However, regardless of whether the AGN

are classified as obscured in the X-ray or optical waveband, there is a clear decrease in the obscured AGN fraction towards higher luminosities. The decrease implies an increase in the opening angle of the torus with luminosity and therefore a decrease in the dust covering fraction, a result that is often interpreted as due to a "receding torus" (see Section 4.1). We note that there is considerable variation between studies in the strength of the decrease in the obscured AGN fraction with luminosity (e.g., see Figure 28 of Toba et al. 2014 for a compilation of multi-wavelength results). Several factors are likely to contribute to the variation in results, including (1) the method adopted to distinguish between obscured and unobscured AGN, (2) the waveband used to select the AGN (i.e., the optical depth and sensitivity towards obscuration), and (3) the range of parameter space used to select the AGN (e.g., across the redshift–luminosity–mass plane). Furthermore, as we discuss in Section 4.1, the primary driver of the obscured AGN fraction may be Eddington ratio rather than luminosity.

In general the evidence for evolution in the obscured AGN fraction with redshift is less secure than with luminosity. An example study is shown in **Figure 10**, which presents the evolution in the X-ray absorbed fraction of Compton-thin and Compton-thick AGN with redshift (Aird et al. 2015b). These constraints were derived from fitting a model to the measurements of the evolving X-ray luminosity functions of X-ray absorbed, X-ray unabsorbed, and Compton-thick AGN using data from deep X-ray surveys; the X-ray luminosity function is the measurement of the space density of AGN as a function of X-ray luminosity, taking into account the X-ray selection function. There is considerable uncertainty in the measured redshift evolution in the obscured AGN fraction. However, overall, the studies broadly agree that the obscured fraction of distant AGN is at least comparable with that found locally and may increase with redshift (e.g., Ueda et al. 2014; Buchner et al. 2015), which could be driven by the increase in the star-formation rate and cold-gas fraction of galaxies with redshift (see Madau & Dickinson 2014 for a recent review).

4. The Physical Nature of Obscuration in AGN

The previous sections illustrate the ubiquity of obscuration in AGN and the diversity of the associated observational signatures. As we discuss below, AGN obscuration is intimately connected to both the fueling of the SMBH (through inflows of gas) and "feedback" (produced by the radiative and mechanical power of the AGN). To understand this connection, we require knowledge of the nature of the obscuring material: the scales, densities, composition, kinematics of the obscuring clouds, and the physical processes that produce them. A number of studies have treated AGN obscuration as dominated by a single regime (most often on the scale of a torus; e.g., Davies et al. 2015; Mateos et al. 2016, 2017), but it is increasingly clear that obscuration can occur on a range of scales and physical conditions. Furthermore, time-varying obscuration has been invoked in models of SMBH-galaxy co-evolution to explain the SMBH-galaxy relationships and the observed connection between AGN and starburst activity (e.g., Di Matteo, Springel & Hernquist 2005; Hopkins et al. 2008; Alexander & Hickox 2012). In this section we will focus on three main regimes of obscuration illustrated in **Figure 11**: (1) the nuclear "torus" posited by AGN unification models, (2) circumnuclear gas associated with central starbursts, and (3) galaxy-scale material associated with galaxy disks and mergers.

An important consideration when comparing these different regimes is the characteristic obscuring column densities that can be associated with each scale. In the simplified case

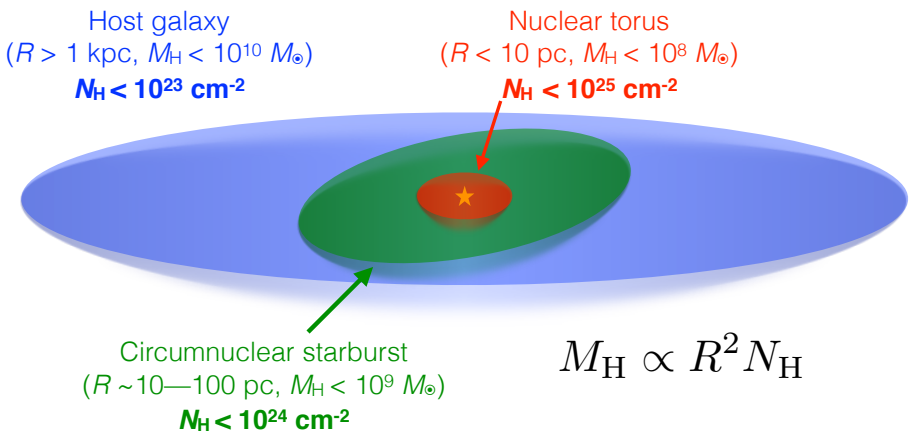

Figure 11

A schematic representation of the different scales of AGN obscuration considered in Section 4, for a Milky Way-type galaxy in the local Universe. For the vastly simplified assumption of constant density, for a given gas mass $M_{\rm H}$, the typical column density $N_{\rm H}$ to the nucleus decreases with size scale as R^{-2}; the heaviest obscuration thus tends to occur on the smaller scales, although larger-scale Compton-thick obscuration can occur in discrete events such as galaxy mergers (Section 5.1) or at high redshifts where the gas fraction in galaxies is large (Section 5.2).

of a hydrogen cloud with constant number density $n_{\rm H}$ distributed over a sphere of radius R, the column density will be $N_{\rm H} = n_{\rm H} R$ and the gas mass will be, in terms of the mass of the hydrogen atom $m_{\rm H}$, $M_{\rm gas} = m_{\rm H} n_H \frac{4}{3}\pi R^3$, such that $M_{\rm H} \propto N_{\rm H} R^2$. Thus for a given mass of gas, $N_{\rm H} \sim R^{-2}$, suggesting that the highest column densities will occur on relatively small scales and therefore that only modest amounts of obscuration can be expected over larger scales for a reasonable mass of gas, as illustrated in the schematic in **Figure 11** (see also Buchner & Bauer 2017). (We note however that instabilities and disturbances such as galaxy mergers can significantly increase the gas density on ∼100 pc to kpc scales, and temporarily produce larger columns along some lines of sight, as discussed in Section 5.1.) In what follows, we will discuss the different regimes of obscuration in the context of observational and theoretical constraints on the typical values of $N_{\rm H}$.

4.1. The nuclear torus and the unified AGN model

As discussed in Section 1, in the physical model for the AGN central engine comprises of a small-scale, broadly axisymmetric structure of dust and gas that surrounds the SMBH, accretion disk, and BLR clouds, and obscures them along some lines of sight (e.g., Antonucci 1993; Urry & Padovani 1995; Netzer 2015). This "unified AGN model" has been remarkably successful at explaining a number of properties of individual AGN (such as the existence of hidden BLRs in some Seyfert 2s; see Section 2.1.2) and of the demographics of the AGN population as a whole (such as the correlation between the X-ray luminosity produced by the accreting SMBH and the mid-IR luminosity that is reprocessed in the torus). However, in recent years it has become clear that the simplest models of the torus that posit a smooth, symmetric "donut"-like structure are inconsistent with observations, as discussed

in Section 2.3. Recent reviews by Netzer (2015) and Ramos Almeida & Ricci (2017) give a comprehensive treatment of the status of the unified AGN model and its successes and challenges; here we will give a brief overview of some of the key points.

4.1.1. The basic torus properties are well-constrained. It is well-established that the inner regions of the obscuring torus are relatively compact (< 1 pc), from near- and mid-IR measurements of reverberation time lags (e.g., Suganuma et al. 2006; Vazquez et al. 2015) and spatially resolved emission from dust using mid-IR interferometry (e.g., López-Gonzaga et al. 2016). The radii of these mid-IR detected structures (assumed to be the AGN torus) closely follow a relationship with AGN luminosity of $r_{\rm torus} \propto L^{1/2}$ that is remarkably consistent with the predicted sublimation radius for graphite dust (e.g., Barvainis 1987; Burtscher et al. 2013)) that is expected to represent the inner edge of the torus. A natural scale for the outer edge of the torus is the gravitational sphere of influence of the SMBH (within which the SMBH dominates the gravitational field), which will broadly correspond to a radius of $\sim$10 pc for nearby systems (e.g., see Section 2.2 of Alexander & Hickox 2012). Observations of the outer regions of the torus have come from mid-IR imaging (e.g. Asmus, Hönig & Gandhi 2016) and studies using molecular lines (e.g., García-Burillo et al. 2016), although the precise outer edge of the torus may be difficult to distinguish from a nuclear starburst disk, as discussed in Section 4.2. The wide observed range of obscuring $N_{\rm H}$ in X-ray studies of AGN suggest a range of column densities through the torus, although the ubiquity of Fe Kα reflection features in AGN X-ray spectra (Section 2.2) suggests that in general, AGN tori are Compton-thick along some lines of sight.

4.1.2. The torus is clumpy. As discussed in Section 2.3, a broad range of evidence points to the torus being highly inhomogeneous in density, temperature, and composition, so that its overall structure is clumpy rather than smooth. One important piece of observational evidence pointing toward a clumpy structure comes from high-resolution mid-IR imaging. Models for smooth tori consistently predict weaker mid-IR emission for edge-on (Type 2) systems due to the torus itself having a large optical depth in the mid-IR, so that its emission is anisotropic (e.g., Fritz, Franceschini & Hatziminaoglou 2006). For a clumpy torus, we expect to observe only the surfaces of the optically-thick clumps, which can be illuminated deep within the torus due to the optically thin lines of sight through the gaps between the clumps. This scenario produces mid-IR emission that is much less dependent on orientation (e.g., Nenkova et al. 2008; Stalevski et al. 2012), in agreement with the remarkably tight observed relationship between X-ray and mid-IR luminosities that is consistent for both Seyfert 1 and 2 galaxies (e.g., Gandhi et al. 2009; García-Bernete et al. 2016). Further evidence for a clumpy torus comes from observations of Si absorption features in the mid-IR spectrum (Section 2.3.2). A common prediction of models for smooth tori viewed edge-on are deep absorption Si absorption lines (e.g., Fritz, Franceschini & Hatziminaoglou 2006). However a study of local Compton-thick AGN by Goulding et al. (2012, Section 2.3) showed that deep Si absorption is most often associated with larger-scale structures (dust lanes or galaxy merger features) rather than a smooth, small-scale torus. By contrast, high-angular resolution nuclear spectra of face-on, isolated Type 2 Seyferts show shallower Si absorption features that can be naturally produced by clumpy torus models (e.g., Roche et al. 2006; Alonso-Herrero et al. 2016b)

4.1.3. The torus can have a range of covering factors, with dependence on AGN properties. One key parameter of the torus is the opening angle, or equivalently, covering factor (f_C). An estimate of f_C can be obtained for individual sources from detailed modeling of the X-ray spectrum (e.g., Brightman & Nandra 2011) and studies of the ratio of reprocessed (IR) to direct (optical or X-ray) AGN emission (e.g., Toba et al. 2014), while the the average f_C for an AGN population can be inferred from the fraction of sources that are obscured for given AGN parameters (e.g., Lawrence 1991). Individual AGN are observed with opening angles over the full range from 0 to 90 degrees (e.g., Mateos et al. 2016), and sources with larger f_C are statistically more likely to be observed as obscured than unobscured (e.g., Elitzur 2012). Even for AGN of similar mass and luminosity, a broad range of torus properties are observed (e.g., Ramos Almeida et al. 2011; Burtscher et al. 2013).

Despite this broad diversity in the tori of individual AGN, there are general trends in average f_C with various AGN parameters. It has long been observed that the obscured fraction (and thus the average f_C) decreases with AGN luminosity (Section 3), which has been interpreted in terms of receding torus models in which increasingly luminous AGN progressively blow away more of the obscuring material (e.g., Lawrence 1991). Studies of optical and soft X-ray samples have suggested that the obscured fraction drops as low as ∼10% at the highest luminosities (e.g., Lawrence 1991; Hasinger 2008). However, recent studies including more sophisticated modeling of incompleteness and anisotropy in the IR emission indicate a much weaker luminosity dependence, with the obscured fraction remaining as high as 50% even for the highest luminosities (e.g., Stalevski et al. 2016; Mateos et al. 2017). This suggests that while the inner radius of the torus increases with luminosity along with the dust sublimation radius (Section 4.1.1), the covering factor of the torus remains broadly constant at the highest luminosities.

It has recently been suggested that the key parameter determining f_C may not be luminosity but Eddington ratio ($L/L_{\rm Edd}$; Buchner & Bauer 2017; Ricci et al. 2017c), with f_C limited by radiation pressure from the AGN acting on dust (e.g., Fabian, Vasudevan & Gandhi 2008). In a study of local hard X-ray selected AGN, Ricci et al. (2017c) found that $f_C \approx 0.8$ at $L/L_{\rm Edd} < 0.02$ and then drops dramatically at higher $L/L_{\rm Edd}$, independent of AGN luminosity. In this picture, the minimum f_C of ≈30% at $L/L_{\rm Edd} > 0.5$ is set primarily by the covering factor of Compton-thick material along the equatorial plane of the torus. A strong dependence of f_C on $L/L_{\rm Edd}$ indicates that most of the obscuring material is within the gravitational sphere of influence of the SMBH, suggesting that (at least for the local AGN in their sample) that a compact torus-like structure is the dominant source of obscuration.

4.1.4. The torus is dynamic. Any structure surrounding an accreting SMBH exists in a complex environment of inflow and outflow. The dynamic nature of the torus is not captured by ad hoc models of smooth or clumpy tori (which are generally static with time) but appear naturally in hydrodynamical models of gas flows around the SMBH. These can produce a variety of broadly axisymmetric structures that may be associated with a torus, including a warped accretion disk (e.g., Jud et al. 2017) or the interaction of inflowing gas with AGN- or starburst-driven winds to produce nuclear structures with large scale heights (e.g., Wada, Schartmann & Meijerink 2016; Hopkins et al. 2016; Hönig & Kishimoto 2017; see **Figure 12**). Some observations of broad absorption line features in AGN spectra have been interpreted as being viewed through axisymmetric outflowing winds that could be interpreted as a torus-like structure (e.g., Gallimore et al. 2016).

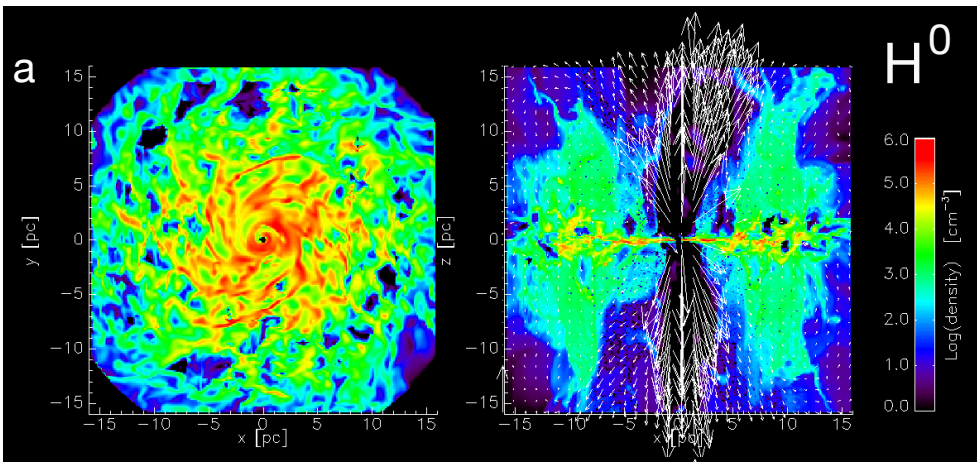

Figure 12

Visualization of the density distribution in a hydrodynamic simulation of flows around a SMBH (Wada, Schartmann & Meijerink 2016), shown face-on (left) and edge-on (right). The simulations illustrate a dynamical radiatively-driven "fountain" that can have obscuration and dust emission properties similar to those observed for some AGN.

4.1.5. The torus may extend in the polar direction, and to large scales. An axiomatic feature of most torus models is that the obscuring gas and dust is broadly symmetric along the rotation axis of the accretion flow. This is motivated the presence of ionization cones observed in NLR gas (e.g., Zakamska et al. 2006; Fischer et al. 2013) and hidden BLRs in some Seyfert 2 galaxies (see Section 2.1.2). However, recent high-resolution observations of a handful of nearby AGN tori using mid-IR interferometry revealed presence of substantial dust emission along the polar direction on pc scales (e.g., Hönig et al. 2012; Tristram et al. 2014; López-Gonzaga et al. 2016). These polar structures can extend to larger scales as shown by imaging observations (e.g., Asmus, Hönig & Gandhi 2016). The physical origin of these features is still unclear, but may be associated with an AGN-driven outflow (e.g., Schartmann et al. 2014). In addition, recent observations have cast some doubt on a compact torus as being the origin of reflected X-ray emission as is often assumed in modeling of obscured AGN (e.g., Murphy & Yaqoob 2009; Brightman & Nandra 2011). Spatially resolved *Chandra* observations have found evidence for Fe Kα lines produced up to ∼kpc away from the nucleus (e.g., Bauer et al. 2015; Fabbiano et al. 2017). Taken together, these results suggest that emission features that have previously been attributed to a compact, axisymmetric torus may often originate from gas and dust with very different geometries. Obscuring material on larger scales may be associated with nuclear starbursts, which are discussed in the next subsection.

4.2. Obscuration by nuclear starbursts

A starburst disk on <100 pc scales is a natural consequence of the significant inflow of gas into the central regions of the galaxy that is required to produce rapid accretion onto the SMBH (e.g., Thompson, Quataert & Murray 2005; Davies et al. 2009). On the scales of the entire galaxy, far-IR observations of AGN have shown that there is a relatively weak

correlation between the AGN luminosity and current (or recent) star formation (e.g., Rosario et al. 2012; Stanley et al. 2015). However, these relationships are found to become tighter when measured over smaller spatial scales (e.g. Diamond-Stanic & Rieke 2012; Esquej et al. 2014), confirming that accreting SMBHs often have a substantial reservoir of gas within the central 100 pc that can fuel a starburst disk.

Such gas is generally kinematically decoupled from the larger galaxy disk, and radiation pressure can cause the starburst disk to expand to a large scale height (e.g., Thompson, Quataert & Murray 2005; Hopkins et al. 2016). Sampling all lines of sight, starburst disks can produce $N_{\rm H}$ distributions that are broadly consistent with observations of the AGN population (Ballantyne 2008; Hopkins et al. 2016; Gohil & Ballantyne 2017). As per the discussion in Section 4.1.1, Compton-thick obscuration in these models is generally limited to small-scale structures (<1 pc for a 3×10^7 $M_\odot$ SMBH) that are difficult to distinguish from a torus. However, Compton-thin obscuration by starburst disks on larger (>10 pc) scales may contribute significantly to the total population of obscured AGN.

4.3. Obscuration by galaxy-scale material

In addition to structures directly related to accretion flows onto the SMBH, obscuration can be produced by gas on the scales of the entire galaxy (>kpc). In a cosmological context, large-scale obscuration is common to models in which SMBH-galaxy co-evolution is driven by galaxy mergers, whereby the gas flows onto the SMBH are connected to galaxy-scale disturbances associated with galaxy-scale merger-driven torques (e.g., Di Matteo, Springel & Hernquist 2005; Hopkins et al. 2008; Alexander & Hickox 2012). In this "evolutionary" picture, the earliest phases of rapid SMBH growth are surrounded by powerful starbursts and shrouded in dust clouds produced by the merger, followed by a "blowout" due to radiative feedback of the AGN that produces an unobscured quasar. Motivated by these theoretical expectations, a number of observational studies have explored the question of whether AGN obscuration can be associated with galaxy-scale structures rather than a nuclear torus or starburst disk.

One approach to identifying galaxy-scale obscuration in AGN is to search for links between obscuration and disturbed or merger morphologies of the host galaxies. From an observational perspective, the merger-AGN connection has been controversial, with some studies suggesting a strong connection, others showing no relationship, and some suggesting a dependence on AGN luminosity (e.g., Koss et al. 2010; Treister et al. 2012; Villforth et al. 2017). Recent results indicate clearly that merging galaxies are more likely to host AGN than isolated galaxies with otherwise similar properties (e.g., Ellison et al. 2013; Weston et al. 2017; Goulding et al. 2017), but whether these mergers are associated with obscuration remains unsettled. For low-luminosity nearby systems, the excess of AGN in mergers is significantly stronger for *WISE*-selected IR AGN than (presumably less-obscured) optically-selected AGN (Satyapal et al. 2014), although the *WISE* color-selected AGN may suffer contamination from low-metallicity starbursts (Hainline et al. 2016). Studies of IR-selected quasar hosts at $z \sim 1$–2 show no clear connection between merger morphology and obscuration (Farrah et al. 2017), and similar results were found for a X-ray selected AGN at $z \sim 2$ (Schawinski et al. 2011; Kocevski et al. 2012). However, recent studies report a possible connection between galaxy mergers and Compton-thick AGN obscuration (Kocevski et al. 2015; Ricci et al. 2017a). While the obscuring material in these studies is modeled to have a small-scale torus geometry, in principle the characteristic X-ray features

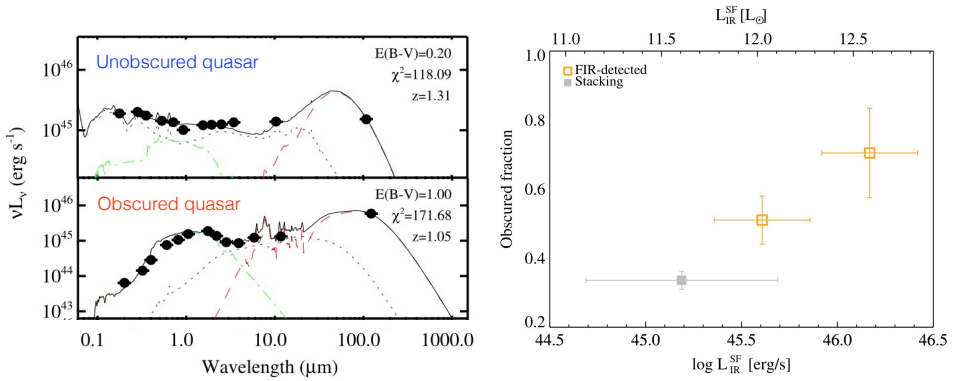

Figure 13

The connection between obscuration and star formation in mid-IR luminous quasars, adapted from Chen et al. (2015). The left panel shows fits to the optical–FIR fits (including *Herschel* data) of an unobscured and obscured quasar identified using mid-IR and optical photometry (Hickox et al. 2007; Chen et al. 2015). Obscured quasars in this sample exhibited stronger far-IR (cold dust) emission compared to their unobscured counterparts; the right panel shows that the fraction of obscured AGN rises significantly with far-IR luminosity, suggesting a connection between AGN obscuration and larger-scale star-forming dust, as discussed in Section 4.3.

might be produced by reflection off clouds on larger scales associated with the merger (e.g., Levenson et al. 2002, see Section 4.1.5). For the population of reddened quasars (which exhibit a visible but highly reddened AGN continuum and represent some of the most luminous known AGN; see Section 2.1) a very high fraction (∼80%) are associated with galaxy mergers and disturbances (e.g., Glikman et al. 2015). Powerful, heavily-obscured *WISE*-selected quasars at $z \sim 2$ (e.g., Assef et al. 2015) also exhibit a large fraction of mergers (Fan et al. 2016). These results are suggestive of a link between mergers and powerful obscured AGN, but further work is needed to confirm this phenomenon.

In an evolutionary scenario, the same galaxy-scale dust and gas that obscures the AGN may also be expected to produce enhanced star formation. Any distinction between the star-forming properties of obscured and unobscured AGN immediately rules out the simplest unified AGN models, in which obscuration is purely due to orientation of the dusty torus. Far-IR and submm studies of luminous quasars show that obscured sources exhibit stronger emission from cold dust; this conclusion holds for obscuration measured in X-rays (e.g., Page et al. 2004, 2011) and also from IR-optical SEDs (e.g., Chen et al. 2015). Chen et al. (2015) furthermore showed that the fraction of quasars that are obscured increased strongly with far-IR luminosity (**Figure 13**), consistent with a picture in which obscuration in luminous AGN is frequently associated with galaxy-scale dust. We emphasize, however, that these studies focused primarily on powerful quasars; for less luminous AGN classified as obscured or unboscured in the X-rays or optical, no comparable difference in average far-IR emission is observed (Merloni et al. 2014). These results suggest that a connection between obscuration and galaxy-scale star-forming material may be most prevalent in powerful AGN.

A final piece of the evolutionary puzzle comes from spatial correlation studies, which provide a robust statistical measure of the large-scale structures (i.e., dark matter halos) in which galaxy and AGN reside, independent of systematics in measurements of galaxy

or AGN properties (e.g., Berlind & Weinberg 2002). Differences in the host halo masses between AGN types would rule out the simplest unified AGN models. Comparisons of obscured and unobscured AGN clustering have engendered significant debate, with some studies showing stronger clustering for obscured AGN, others for unobscured AGN, and still others showing no difference (e.g., Hickox et al. 2011; Allevato et al. 2011; Mendez et al. 2016). The large samples of $> 10^5$ quasars identified with *WISE* have enabled high-precision measurements, consistently showing stronger clustering for the obscured population (e.g., Donoso et al. 2012; DiPompeo et al. 2014). This difference has been confirmed through independent cross-correlations of the quasar positions with lensing maps derived from the cosmic microwave background (e.g. DiPompeo et al. 2015, 2017a). These results can be explained qualitatively with a model in which the obscured quasars have SMBHs that are undermassive relative to their halos and are "catching up" to their final mass, consistent with an evolutionary scenario (DiPompeo et al. 2017b).

5. Implications for Obscured AGN in Observational Cosmology

The previous section demonstrates that, while most AGN obscuration is likely to occur in nuclear regions within the sphere of influence of the SMBH (Section 4.1), a significant fraction of the obscuration may originate on larger scales (Sections 4.2 and 4.3). Obscuration during discrete events such as starbursts or galaxy mergers point to a link between SMBH growth and the cosmological formation of galaxies and large-scale structures. In this section we explore three of the implications of obscured SMBH growth for observational cosmology: (1) The SMBH-galaxy evolutionary sequence, (2) Obscured SMBH growth in the early Universe, and (3) The "missing" AGN population and the radiative efficiency of SMBH accretion.

5.1. The evolutionary sequence and the SMBH-galaxy connection

As discussed in Section 1.2, connections between SMBHs and galaxies in their cosmic evolution have attracted a great deal of interest, motivated in part by observations of concurrent AGN and starbursts in well-studied local systems (e.g., Sanders & Mirabel 1996; Farrah et al. 2003), statistical connections between AGN activity and star formation or stellar mass in extragalactic surveys (e.g., Chen et al. 2013; Azadi et al. 2015), and observed correlations between SMBH masses and host galaxy properties (velocity dispersion, stellar mass, etc.; McConnell & Ma 2013; Kormendy & Ho 2013; Graham 2016). The growth of SMBHs releases enormous amounts of energy in the form of radiation, outflows, and relativistic jets that can significantly influence the evolution of the host galaxies (e.g., Alexander & Hickox 2012; Fabian 2012). Many galaxy formation models require energy input from AGN to produce the observed population of quiescent galaxies (e.g., Bower et al. 2006; Dubois et al. 2016). Ultimately, there is likely to be a complex interplay between SMBH and galaxy growth, in which AGN activity follows or enhances the growth of stars in some cases, and shuts off or prevents new star formation in others (see Harrison 2017, for a review).

An important role in many models of SMBH-galaxy co-evolution is played by obscured AGN. Some models posit rapid phases of galaxy and SMBH growth triggered by mergers, interactions, or violent instabilities that can also disrupt the gas content of the galaxy and shroud the AGN (e.g., Sanders et al. 1988; Hopkins et al. 2008). The majority of the SMBH and galaxy growth is predicted to occur in an early obscured phase (e.g., Blecha et al. 2017;

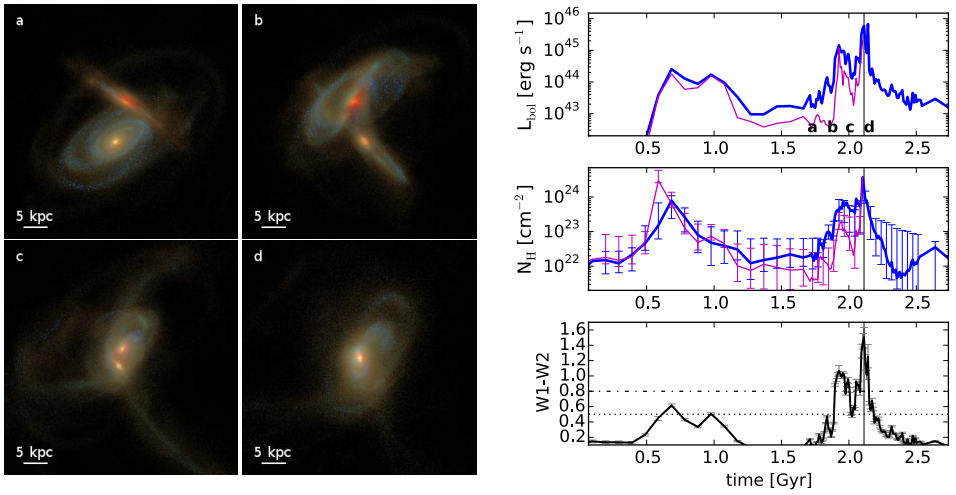

Figure 14

An illustration of SMBH fueling and obscuration during a galaxy merger (Blecha et al. 2017). The left panel shows images of simulated galaxies in four different stages of a merger, with the time dependence of AGN $L_{\rm bol}$, $N_{\rm H}$, and *WISE* W1–W2 color are shown in the right column. The coalescence of the galaxies and SMBHs produces a spike in SMBH accretion and $L_{\rm bol}$, along with a redder W1–W2 color and a jump in $N_{\rm H}$ that reaches approximately Compton-thick ($N_{\rm H} \sim 10^{24}$ cm^{-2}) level.

Figure 14), followed by a "blowout" phase in which AGN feedback both limits SMBH growth and ejects gas from the galaxy potential, quenching the starburst and preventing further star formation (e.g., Ishibashi & Fabian 2016). In this picture the period of obscured AGN activity represents the key phase for building up the mass of the SMBH, while the later AGN luminosity limits the growth and sets the relationship between the SMBH and galaxy. The impact of the AGN on surrounding gas can be observed in outflows, heating, and turbulence in molecular, atomic, and ionized gas (e.g., Greene et al. 2011; Harrison et al. 2014; Feruglio et al. 2015).

However, whether galaxy and SMBH evolution is primarily driven by discrete, dramatic phases of evolution remains unclear. Some studies have suggested that the relationships between SMBHs and galaxies progress slowly over cosmic time, with the fueling (and obscuration) of AGN being primarily a stochastic process (e.g., Cisternas et al. 2011; Mullaney et al. 2012), so that obscured AGN do not represent an especially important phase in SMBH growth or feedback. It may also be possible that the importance of obscured AGN activity depends strongly on the type of galaxy and its evolutionary history; since massive ellipticals and galaxy bulges have old, α-enhanced stellar populations that formed in rapid starbursts (e.g., Zhu, Blanton & Moustakas 2010; McDermid et al. 2015), obscured AGN activity may be more important in the formation of these systems than in disk-dominated galaxies with more quiescent SF histories (e.g., Ishibashi & Fabian 2017).

A key clue in uncovering the role of obscured AGN in the cosmological growth of SMBHs is the determination of whether obscuration is connected with processes in the nuclear torus (small enough to be decoupled from the broader galaxy formation) or on the scale of

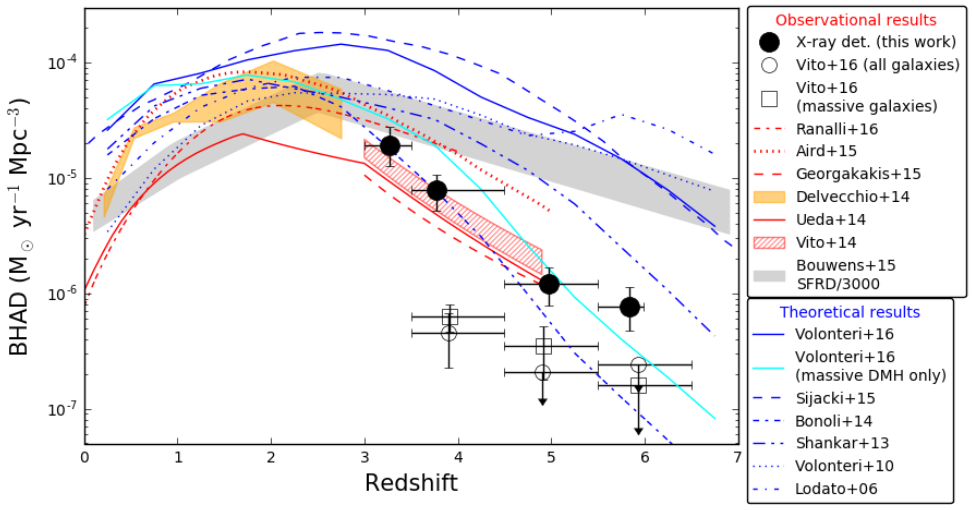

Figure 15

Evolution in the AGN X-ray luminosity density at high z, as determined through *Chandra* Deep Field Observations (Vito et al. 2018). The rapid drop-off of the luminosity density (shown by the black points) suggests that SMBH growth falls with redshift faster than does star formation (shown by the gray filled region). This fast evolution rules out a number of SMBH evolution models (shown as blue lines); this tension may be resolved by the existence of a highly-obscured AGN population at these redshifts.

the galaxy. Further observations are required to determine the fractions of AGN that are obscured due to material on "torus" and "galaxy" scales (as discussed in Section 4.3), and to determine the sub-populations of galaxies for which obscured AGN may play a particularly important role.

5.2. The evolution of obscured SMBHs at high redshift

If AGN obscuration is connected to the gas content of the host galaxy, then we may expect obscuration to be enhanced at higher redshift, where the fraction of mass of galaxies in atomic or molecular gas is far higher than in the local Universe (e.g., Carilli & Walter 2013). As discussed in Section 3, X-ray observations have shown hints that the obscured fraction may increase with redshift. For a galaxy with a high enough mass of gas, even large-scale (∼kpc) obscuring clouds can be heavily absorbing or even Compton-thick, so X-ray observations may miss an increasing fraction of the SMBH growth at higher redshifts. Powerful, mid-IR-bright obscured quasars at $z \sim 2$ frequently show weak or absent X-ray detections even in deep observations (Stern et al. 2014; Del Moro et al. 2016), suggesting that the Compton-thick fraction for these AGN are ∼25–50%, comparable to local samples (see Section 3) but at higher AGN luminosities. If this high Compton-thick fraction is also present for lower luminosity AGN at high redshift, a substantial fraction of the SMBH growth at high redshift might not be captured by current X-ray observations (see Section 5.3 for the implications of this on the global radiative efficiency).

The question of "missing" obscured AGN is particularly interesting at high redshift

($z > 3$). Luminous quasars with $M_{\rm BH} > 10^9$ $M_\odot$ are observed to emerge at $z = 6$–7 (e.g., Mortlock et al. 2011; Wu et al. 2015) and increase in space density to lower redshifts with a peak at $z \sim 2$ (e.g., Kelly et al. 2010). The growth of lower-mass SMBHs that ultimately power these massive quasars can be probed with deep X-ray studies of lower-luminosity AGN (see Volonteri 2010, for a review). Recent studies of the deepest *Chandra* fields reveal a steep drop-off in the X-ray selected AGN space density at $z > 3$, with the evolution strongest for soft X-ray luminosity $< 10^{44}$ erg s^{-1} (Vito et al. 2018; see **Figure 15**). If the X-ray observations do probe the complete radiative output of AGN at these redshifts, then models of SMBH "seeds" may encounter problems with insufficient SMBH growth to produce the observed massive quasars at lower redshifts. One potential solution is if the AGN are heavily obscured, which would allow for the presence of many more growing SMBHs that lie below the *Chandra* detection (or stacking) thresholds (e.g., Novak 2013; Vito et al. 2018).

At the highest redshifts, obscured accretion is an essential component to some of the SMBH seed models themselves. In particular "direct collapse" models posit the growth of early SMBHs in gas-rich dark matter halos (e.g., Volonteri & Begelman 2010; Mayer et al. 2010) and the accretion process in these models implies high covering factors with Compton-thick absorption. In these models, the earliest growth of SMBHs is necessarily heavily obscured, although some signatures of these direct-collapsing systems may be observable through reprocessed IR radiation (e.g., Natarajan et al. 2017).

5.3. Obscured AGN, the cosmic X-ray background, and the radiative efficiency of black hole accretion

The presence of a population of heavily obscured AGN has important consequences for the fundamental physics of SMBH accretion (in particular the radiative efficiency), and the corresponding origin of the cosmic background radiation. As first proposed by Soltan (1982), the total radiation emitted by SMBHs over cosmic time provides a powerful clue to the accretion process that produces the population of SMBHs observed at low redshift. The concept is elegantly simple: The total radiation density produced by SMBHs ($U_{\rm T}$) is equal to the product of the mass density of SMBHs in the local Universe (assumed to have been accumulated via accretion) $\rho_{\rm SMBH}$ and the radiative efficiency ϵ. Including a factor of $1 - \epsilon$ to account for the mass-energy lost as radiation, this relationship can be written as:

$$\rho_{\rm SMBH} c^2 = U_{\rm T} \frac{1-\epsilon}{\epsilon} \quad (1)$$

A number of early studies used the space density of optically-selected unobscured quasars to estimate ϵ (e.g., Yu & Tremaine 2002). These studies included no obscured AGN and so naturally produced on a lower limit on $U_{\rm T}$, or required an estimate of the fraction of radiation that was obscured, as well as an estimate of the optical bolometric correction (the scale factor $k_{\rm opt}$ to convert from optical radiation density $U_{\rm opt}$ to total radiation density; $U_{\rm T} = k_{\rm opt} U_{\rm opt}$). Subsequent studies attempted to directly account for the obscured sources through measurements of the cosmic X-ray background (CXB); sensitive X-ray observations have confirmed that the CXB is dominated by emission from individual AGN (e.g., Bauer et al. 2004; Hickox & Markevitch 2006, see Brandt & Alexander 2015 for a recent review) and dominate the CXB even to $E > 10$ keV (e.g., Aird et al. 2015a; Harrison et al. 2016). Successful CXB synthesis models universally require a population of obscured AGN to produce the observed peak in the spectrum at $E \sim 30$ keV (Gilli,

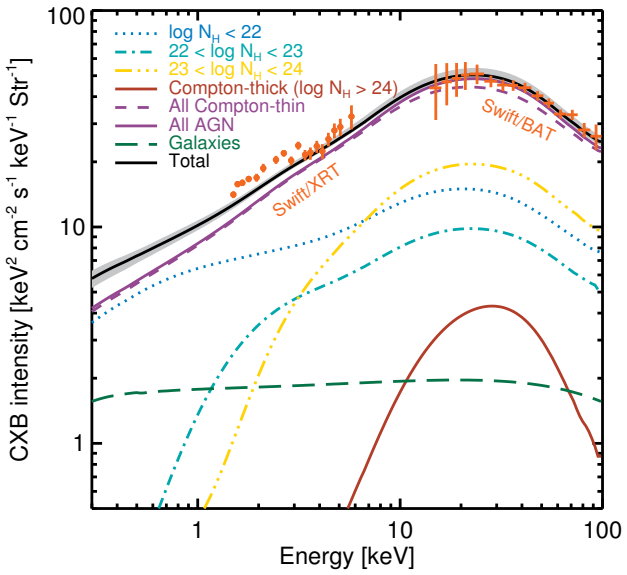

Figure 16

Synthesis model of the cosmic X-ray background (CXB; Aird et al. 2015b), showing the contributions to the CXB from unobscured AGN (blue dotted line) and obscured AGN with varying levels of $N_{\rm H}$. The high-energy peak of the CXB is dominated by obscured sources, with a significant contribution from Compton-thick AGN (thick red line). CXB synthesis models have been used to estimate the SMBH radiative efficiency ϵ, but may not account for the presence of an extremely obscured population (with $N_{\rm H} > 10^{25}$ cm^{-2}) that does not contribute significantly to the CXB (Section 5.3).

Comastri & Hasinger 2007; Treister, Urry & Virani 2009; Ballantyne et al. 2011; Akylas et al. 2012; Ueda et al. 2014; Aird et al. 2015b, see **Figure 16**). After correcting the total CXB radiation for absorption (either empirically, or through AGN synthesis models), and assuming an X-ray bolometric correction (k_T), it can be used to estimate ϵ (e.g., Fabian & Iwasawa 1999).

In recent years there has been substantial progress in understanding the cosmic synthesis of SMBHs. Large obscured AGN populations have been discovered that could substantially increase U_T (Section 3) and updates to the local SMBH mass density have come from new dynamical measurements of SMBH masses and re-assessments of relationships between SMBH masses and galaxy properties (e.g., Kormendy & Ho 2013). These new scaling relations significantly increased the estimate of $\rho_{\rm SMBH}$, by up to a factor of 5; for the same value of U_T, this would lead to a corresponding decrease in ϵ that would fall uncomfortably far below the theoretically expected value of $\epsilon \approx 0.1$ (Kerr 1963; Shapiro & Teukolsky 1983; see Section 1).

However, in these analyses one fundamental uncertainty is the fraction of AGN that are so heavily obscured that they contribute little or nothing to the observed radiation fields used to compute U_T and thus ϵ (see e.g., Martínez-Sansigre & Taylor 2009; Novak 2013). The total obscured fraction and $N_{\rm H}$ distribution is often inferred from local optical or X-ray

studies (e.g., Burlon et al. 2011; Ricci et al. 2017b). However, in principle a substantial fraction of sources may be missed through extremely heavy absorption that is not accounted for in the selection function (as discussed in Section 2), and the $N_{\rm H}$ distribution may evolve significantly with redshift. The "missing" AGN population could therefore contribute a substantially higher fraction of the total SMBH growth than is assumed based on local studies. Due to energy conservation, the radiation from such sources must ultimately emerge at far-IR and submm wavelengths as it is reprocessed into thermal emission from cold dust. A census of the AGN population obtained from fitting broad-band SEDs (including far-IR data from *Herschel*) suggests that the evolution of the luminosity function of AGN identified in the IR is comparable to that determined from other wavebands (Delvecchio et al. 2014). However, the signal from extremely heavily buried AGN may be challenging or impossible to distinguish from emission powered by star formation processes that completely dominate the IR background at > 10 μm (Shi et al. 2013). Comastri et al. (2015) showed that the total radiation output from accreting SMBHs could be increased by a factor of $\sim$2 in the form of extremely Compton-thick, X-ray faint AGN without violating constraints in the X-ray and IR backgrounds. This, in turn, would increase ϵ by a similar factor, potentially resolving tension with theoretical expectations.

6. Conclusions and future prospects

In this review we have highlighted progress in identifying and characterizing obscured AGN, and have detailed the associated physical insights related to the accretion process onto SMBHs and its cosmological implications. Observationally, the combination of sensitive observations over a broad range of wavelengths (particularly the mid-IR and hard X-rays) have enabled a much improved census of the population of growing SMBHs in the past decade (Sections 2 and 3). Major recent advances include better understanding of the geometry and properties of the obscuring "torus" (Section 4.1), evidence for obscuration on host galaxy scales and connections to galaxy evolution (Sections 4.2, 4.3 and 5.1), direct measurements of the contribution of AGN to the hard CXB (Section 5.3), and the discovery of a (possibly large) population of very heavily obscured AGN that may be particularly important at high redshift (Section 5.2). These results suggest an important role for obscured accretion in the growth histories of SMBHs (both in the rapid evolution of massive galaxies, and in the early growth of "seed" SMBHs), and indicate that while the bulk of obscuration appears to occur in compact regions within the sphere of influence of the SMBH, obscuration occurs over a wide range of scales and physical conditions. In this final section we discuss how our understanding of obscured AGN wil be further improved with future observational facilities and developments in theoretical models, and suggest some open questions that provide particularly promising opportunities for progress.

6.1. Forecasts for future facilities

The coming decades will see an impressive array of new observational resources that will enhance our abilities to detect and characterize obscured AGN. Here we will discuss the prospects for a handful of upcoming or proposed facilities in each of the wavebands discussed in Section 2.

6.1.1. UV–Near-IR. Spectroscopy provides the most widely-applicable method for studying obscured AGN in the optical and NIR (Section 2.1.2). From the ground, new large-scale multi-object spectrographs in the optical and near-IR such as DESI[2] (DESI Collaboration et al. 2016), 4MOST[3] (de Jong et al. 2014), and Subaru PFS[4] (Takada et al. 2014) will identify and characterize huge numbers of obscured AGN, including rest-frame optical lines out to $z \sim 3$–4. In addition, new surveys with integral field units such as SAMI[5] (Croom et al. 2012), CALIFA (Sánchez et al. 2012)[6], and MaNGA[7] (Bundy et al. 2015) are enabling detailed spatially resolved studies of NLR ionization and kinematics. From space, *JWST*[8] and *WFIRST*[9] will provide extremely sensitive infrared spectroscopy with high spatial resolution, allowing characterization of the emission features in rest-frame optical (which are critical for AGN diagnostics; Section 2.1) and also host galaxy properties of obscured AGN out to high redshift. Further into the future, the 30-m class telescopes such as GMT[10], TMT[11], and E-ELT[12] will perform high sensitivity observations of obscured AGN to high redshifts, and the LUVOIR[13] and HABEX[14] concept space missions would carry out sensitive optical spectroscopy and imaging of obscured AGN with extremely high angular resolution. Finally, LSST[15] will provide extremely deep, wide-field optical imaging that, while not able to efficiently select obscured AGN, will be powerful for the characterization of AGN host galaxies and identifying rare changing-look AGN (see Section 2.1.2).

6.1.2. X-rays. For statistical studies of obscured AGN, new generations of X-ray telescopes will enable deep, wide-area surveys resulting in very large samples of AGN. The *eROSITA* mission[16] will identify millions of AGN over the whole sky (Merloni et al. 2012), including a significant number of obscured sources (with follow-up spectroscopy from 4MOST), although its ability to probe the complete obscured AGN population will be limited by its energy response, which drops off more quickly at energies > 3 keV when compared to *Chandra* and *XMM*. Further into the future, the *Athena* mission[17] (Barcons et al. 2015) will enable sensitive X-ray imaging spectroscopy with sensitivity to $\approx$12 keV, and over a wide 40' field of view. *Athena* surveys will reach, over a large area, a confusion-limited source detection flux limit approximately equal to that of the *Chandra* Deep Fields (e.g., Xue et al. 2011; Luo et al. 2017), and will allow extremely sensitive spectroscopy of faint and high-redshift AGN, providing a significant leap forward in the selection of distant heavily

[2]http://desi.lbl.gov/
[3]https://www.4most.eu/
[4]http://pfs.ipmu.jp/
[5]https://sami-survey.org/
[6]http://califa.caha.es
[7]http://www.sdss.org/surveys/manga/
[8]https://jwst.nasa.gov/
[9]https://wfirst.gsfc.nasa.gov/
[10]https://www.gmto.org/
[11]http://www.tmt.org/
[12]https://www.eso.org/sci/facilities/eelt/
[13]https://asd.gsfc.nasa.gov/luvoir/
[14]https://www.jpl.nasa.gov/habex/
[15]https://www.lsst.org/
[16]http://www.mpe.mpg.de/eROSITA
[17]http://www.the-athena-x-ray-observatory.eu/

obscured and CT AGN. The *Lynx* concept mission[18] (with higher spatial resolution) would probe up to two orders of magnitude fainter with imaging and spectroscopy of obscured AGN out to the highest redshifts and providing constraints on SMBH seed models (see Section 5.2) and imaging of obscured AGN nuclei to better constrain the nature of obscuring and reflecting material (see Section 4.1). Among a number of proposed smaller X-ray missions, a particularly powerful tool for studying obscured AGN is *HEX-P*[19], which would build on the success of *NuSTAR* with higher-resolution imaging observations at $E > 10$ keV.

For detailed studies of individual obscured AGN, the upcoming *XARM* mission[20] will provide calorimeter observations with exquisite energy resolution to measure the strength and profile of the Fe Kα line, Compton shoulder, and other features to constrain the obscuring geometry. To best take advantage of *XARM*s capabilities, simultaneous observations at harder (>10 keV) X-rays (for example with *NuSTAR* if it is still operational) are required to provide the broad energy coverage for constraining the strength and shape of the Compton-reflected continuum. Finally, we will soon see the emergence of X-ray polarization measurements, first with the *IXPE* mission[21] and potentially on longer timescales with *XIPE*[22]. Polarization provides a unique capability for studying scattering and reflection, and so can offer new constraints on the geometry of the nuclear regions of obscured AGN (Marin et al. 2018).

6.1.3. Mid-IR. Dramatic breakthroughs in the mid-IR studies of obscured AGN will come from *JWST*, which will greatly improve the sensitivity of mid-IR spectroscopy (for characterizing optically faint or X-ray faint AGN and identifying extremely weak or buried sources; see Section 2.3.2) and photometry (for identifying obscured AGN in faint, high-redshift galaxies; see Section 2.3.1). For extremely high angular resolution observations, the new MATISSE instrument[23] on the VLT Interferometer (with corresponding NIR imaging from the GRAVITY instrument[24]) will enable superior imaging capabilities for follow up imaging studies of the resolved dust emission in nearby AGN (see Section 4.1).

6.1.4. Far-IR–radio. ALMA[25] will continue to make leaps forward in our understanding of obscured AGN; in particular, the development of new submm line diagnostics (e.g., Aalto et al. 2015; Imanishi, Nakanishi & Izumi 2016; See Section 2.4.1) will enable the identification of excitation due to AGN in even the most heavily buried systems, particularly with anticipated improvements in sensitivity with future ALMA upgrades. ALMA will also be key in constraining spatially-resolved properties of the molecular torus such as the outer radius, gas mass, and kinematics, as discussed in Section 4.1. Sensitive AGN diagnostic studies can also be performed with the LMT[26] and CCAT[27], which reach similar

[18] https://wwwastro.msfc.nasa.gov/lynx/
[19] pcos.gsfc.nasa.gov/studies/rfi/Harrison-Fiona-RFI.pdf
[20] https://heasarc.gsfc.nasa.gov/docs/xarm/
[21] https://ixpe.msfc.nasa.gov/
[22] http://www.isdc.unige.ch/xipe/
[23] https://www.eso.org/sci/facilities/develop/instruments/matisse/.html
[24] https://www.eso.org/sci/facilities/paranal/instruments/gravity.html
[25] http://www.almaobservatory.org/
[26] http://www.lmtgtm.org/
[27] http://www.ccatobservatory.org/

depths to ALMA over wider fields of view, although with lower angular resolution. From space, concept far-IR observatories such as *OST*[28] and *SPICA*[29] would provide sensitive, high-resolution observations of line emission to explore the connection between obscured AGN activity and star formation, in order to constrain obscuration on galaxy scales and test evolutionary models (Sections 4.3 and 5.1). The most exciting potential for future breakthroughs in the radio band comes from the SKA[30] and its prescursor radio telescopes including LOFAR[31], ASKAP[32], MeerKAT[33], MWA[34], and HERA[35]. These observatories are moving toward a dramatic improvement in the sensitivity of deep radio surveys and will eventually allow us to probe, even out to $z = 5$–6 and beyond, faint radio luminosities for which non-jetted sources dominate the AGN number counts. In combination with deep optical and IR surveys, the SKA will enable vastly deeper and more powerful use of the "radio-excess" method, as well as (along with enhanced capabilities with VLBI) directly resolving compact bright compact cores. These will allow for the detection of AGN that are otherwise obscured or swamped by star formation processes (Section 2.4.2).

6.2. Prospects for theoretical models

Our understanding of obscured AGN will also see progress through advances in theoretical models, both on the scale of the accretion flow and the obscuring torus, and in the context of large-scale cosmological models of galaxy formation.

On small scales, our understanding of AGN obscuration has been improved by advances in hydrodynamical simulations that capture the complex, dynamic, and multi-scale nature of the AGN central engine. Better physical prescriptions for feedback (e.g., Hopkins et al. 2016), chemistry (e.g., Wada, Schartmann & Meijerink 2016), and radiative transfer (e.g., Jud et al. 2017) all yield a more complete picture of the physical origin and observational signatures of obscuring material in AGN. Complementary to fully hydrodynamic models, there have also been improvements in phenomenological models of AGN tori (for example, including multi-phase gas consisting of both clumpy and smooth components; e.g., Siebenmorgen, Heymann & Efstathiou 2015; Stalevski et al. 2016) and the associated radiative transfer calculations that provide input for interpreting the observed AGN SEDs. The future will see additional connections between hydrodynamic and phenomenological models. For example simulations can provide a framework for realistic ranges of torus opening angles, cloud sizes and optical depths that can then be used to create phenomenological models for constraining the properties of the observed AGN tori.

On the largest scales, we can make use of galaxy formation models, for which one direct and immediate application will be to better understand the strong selection effects involved in identifying obscured AGN. As illustrated in Sections 1 and 2 and **Figure 4**, selection effects due to obscuration, host dilution, and physical changes in accretion present a complex multi-faced problem, and it can be challenging to reliably invert these effects

[28]https://asd.gsfc.nasa.gov/firs/
[29]http://www.spica-mission.org/
[30]https://skatelescope.org/
[31]http://www.lofar.org/
[32]http://www.atnf.csiro.au/projects/askap/
[33]www.ska.ac.za/meerkat/
[34]http://www.mwatelescope.org/
[35]http://reionization.org/

from any given survey to recover the underlying cosmological AGN population. To address these issues, studies increasingly make use of forward modeling that begin with a known underlying galaxy and AGN population, and model their observational signatures in a range of wavebands. By adjusting the input parameters to match the observational data, it is possible to recover (with some assumptions) a reliable measure of the intrinsic AGN population. This approach has been used successfully in synthesis models that produce the CXB and the local SMBH mass function (e.g., Merloni & Heinz 2008), while also fitting the evolution of the observed XLF. However, in most cases, these models have assumed empirical parameters for the XLF without explicit connection between the AGN and their host galaxies and dark matter halos. Given the importance of host galaxy dilution on AGN selection (see Section 2), and the potentially critical role played by large-scale structures in driving galaxy-SMBH evolution (see Section 5.1), more complete modeling of the AGN population in a cosmological context is warranted. Some studies have included SMBH accretion in cosmological hydrodynamic simulations (e.g., McAlpine et al. 2017; Weinberger et al. 2017), with some success modeling the observed distributions of SMBH mass and AGN luminosity. However, these models necessarily assume simplified sub-grid prescriptions for AGN accretion and feedback (see the discussion in Negri & Volonteri 2017) and due to the computational expense, they are not able to explore a wide range of parameters for the underlying AGN population. Recently, models have added AGN to simulated galaxies that are drawn either from semi-analytic dark matter and galaxy formation simulations (e.g., Jones et al. 2017), or observed distributions in galaxy mass and star formation history (e.g., Weigel et al. 2017). These prescriptions allow for the flexibility to include in galaxies a population of AGN with wide range of underlying parameters, while also modeling the full multiwavelength properties of the AGN including the emission and/or obscuration from the host galaxy. This modeling yields insights into which AGN are not selected in multiwavelength surveys, and provide useful tools for recovering the full population of obscured AGN.

An ultimate goal for theoretical models of obscured AGN would be to perform a simulation over a dynamic range from the size of the galaxy or dark matter halo (>kpc) down to the accretion disk itself, covering all the relevant scales for gas dynamics and obscuration by gas and dust (Section 4). To date, computational limitations have meant that a full self-consistent treatment of the relevant physics over this range of scales has been out of reach. However, recent studies have performed 3D simulations of feeding, feedback, and obscuration from 0.1 pc to 100 pc scales (Hopkins et al. 2016), while simulations of SMBH feeding and feedback can be now performed on a full galaxy scale, with resolution as small as 3 pc (e.g., Gabor & Bournaud 2013; Negri & Volonteri 2017), so a complete treatment across the full range of scales may be on the horizon.

6.3. Outstanding questions

This review has highlighted just a fraction of the exciting observational and theoretical progress that has greatly enhanced our understanding of obscured AGN in recent years. Looking to build on these insights, we conclude with some key outstanding questions:

6.3.1. What is the physical origin of the torus?. The structural properties of the AGN dusty torus (such as a clumpy geometry, and broad range of covering factors, and the existence of dust along the poles) are coming into sharper focus (see Section 4.1). However, there remain

many possible explanations for its formation, including warped accretion disks, AGN-driven winds, and starburst disks. Uncovering the physical origin (or multiple origins) of the torus is an important goal in coming years.

6.3.2. What is the evolution of AGN obscuration and the connection to galaxy formation?. Observations have uncovered hints of evolution with redshift of the fraction of AGN that are obscured (see Section 3), and suggest that some AGN are obscured by evolutionary processes in galaxies (see Section 5.1) that, along with galaxy gas fractions and merger rates, can depend strongly with redshift. A major future objective will be to accurately measure the distribution of AGN obscuration with redshift, luminosity, or Eddington ratio, and to nail down the fraction of obscuration that is produced by galaxy-scale processes as opposed to a nuclear torus. One important clue may come from SMBH mergers identified by the *LISA* gravitational wave observatory[36], which could place important constraints on galaxy and SMBH merger rates and provide signatures of obscured SMBHs that may not be identifiable from electromagnetic signatures.

6.3.3. How do we find the most heavily obscured AGN?. Recent observations have begun to show evidence for a population of extremely heavily obscured AGN with $N_{\rm H} \gg 10^{25}$ cm^{-2}. AGN at these levels of obscuration may exhibit few clear observational signatures (see Section 2) but might still contribute significantly to the global growth of SMBHs (see Section 5.3). Some of the most promising techniques to uncover these sources use long-wavelength observations, for which the opacity is the lowest. For example, submm line diagnostics (see Section 2.4.1) or high-resolution detections of radio cores (see Section 2.4.2) may be critical in uncovering this most heavily obscured AGN population.

6.3.4. What is the role of obscured accretion at the dawn of the first SMBHs?. The rapid early growth of SMBHs from seeds to massive quasar engines is currently an active area of inquiry. Theoretical models, as well as the rapid drop-off in the observed AGN density at high redshift, raise the possibility that a large fraction of the earliest SMBH growth may have been heavily obscured (see Section 5.2). Uncovering this population will be a major motivation for upcoming observatories that seek to understand the ultimate origin of SMBHs.

ACKNOWLEDGMENTS

R.C.H. acknowledges support from the National Science Foundation through AST grant number 1515364 and CAREER grant 1554584, from NASA through grants NNX15AU32H and NNX16AN48G, and from an Alfred P. Sloan Research Fellowship. D.M.A. acknowledges support from the Science and Technology Facilities Council (STFC) for support through grant ST/L00075X/1. We are grateful to Cristina Ramos Almeida, Andrea Merloni, Michael DiPompeo, Lauranne Lanz, and Scientific Editor Luis Ho for valuable suggestions that improved the manuscript. Many of the ideas for the content of this review were developed during the "Hidden Monsters: Obscured AGN and Connections to Galaxy Evolution" workshop at Dartmouth College over August 8–12 2016 and the "Elusive AGN in the Next Era"

[36]https://www.lisamission.org/

workshop at George Mason University over June 12–15 2017. We would like to thank the workshop participants for stimulating talks and discussions!

LITERATURE CITED

Aalto S, Martín S, Costagliola F, González-Alfonso E, Muller S, et al. 2015. *A&A* 584:A42
Aird J, Alexander DM, Ballantyne DR, Civano F, Del-Moro A, et al. 2015a. *ApJ* 815:66
Aird J, Coil AL, Georgakakis A, Nandra K, Barro G, Pérez-González PG. 2015b. *MNRAS* 451:1892–1927
Akylas A, Georgakakis A, Georgantopoulos I, Brightman M, Nandra K. 2012. *A&A* 546:A98
Akylas A, Georgantopoulos I, Ranalli P, Gkiokas E, Corral A, Lanzuisi G. 2016. *A&A* 594:A73
Alexander DM, Bauer FE, Chapman SC, Smail I, Blain AW, et al. 2005. *ApJ* 632:736–750
Alexander DM, Chary RR, Pope A, Bauer FE, Brandt WN, et al. 2008. *ApJ* 687:835–847
Alexander DM, Hickox RC. 2012. *New Astron. Revs* 56:93–121
Allevato V, Finoguenov A, Cappelluti N, Miyaji T, Hasinger G, et al. 2011. *ApJ* 736:99–+
Alonso-Herrero A, Esquej P, Roche PF, Ramos Almeida C, González-Martín O, et al. 2016a. *MNRAS* 455:563–583
Alonso-Herrero A, Esquej P, Roche PF, Ramos Almeida C, González-Martín O, et al. 2016b. *MNRAS* 455:563–583
Alonso-Herrero A, Pérez-Gonz ález PG, Alexander DM, Rieke GH, Rigopoulou D, et al. 2006. *ApJ* 640:167–184
Annuar A, Alexander DM, Gandhi P, Lansbury GB, Asmus D, et al. 2017. *ApJ* 836:165
Annuar A, Gandhi P, Alexander DM, Lansbury GB, Arévalo P, et al. 2015. *ApJ* 815:36
Antonucci R. 1993. *ARA&A* 31:473–521
Antonucci RRJ, Miller JS. 1985. *ApJ* 297:621–632
Asmus D, Hönig SF, Gandhi P. 2016. *ApJ* 822:109
Asmus D, Hönig SF, Gandhi P, Smette A, Duschl WJ. 2014. *MNRAS* 439:1648–1679
Assef RJ, Eisenhardt PRM, Stern D, Tsai CW, Wu J, et al. 2015. *ApJ* 804:27
Assef RJ, Kochanek CS, Brodwin M, Cool R, Forman W, et al. 2010. *ApJ* 713:970–985
Assef RJ, Stern D, Kochanek CS, Blain AW, Brodwin M, et al. 2013. *ApJ* 772:26
Azadi M, Aird J, Coil AL, Moustakas J, Mendez AJ, et al. 2015. *ApJ* 806:187
Baade W, Minkowski R. 1954. *ApJ* 119:206
Baker JG, Menzel DH. 1938. *ApJ* 88:52
Baldwin JA, Phillips MM, Terlevich R. 1981. *PASP* 93:5–19
Ballantyne DR. 2008. *ApJ* 685:787–800
Ballantyne DR, Draper AR, Madsen KK, Rigby JR, Treister E. 2011. *ApJ* 736:56
Baloković M, Brightman M, Harrison FA, Comastri A, Ricci C, et al. 2018. *ApJ* 854:42
Barcons X, Nandra K, Barret D, den Herder JW, Fabian AC, et al. 2015. *Journal of Physics Conference Series* 610:012008
Barmby P, Alonso-Herrero A, Donley JL, Egami E, Fazio GG, et al. 2006. *ApJ* 642:126–139
Barvainis R. 1987. *ApJ* 320:537–544
Bauer FE, Alexander DM, Brandt WN, Schneider DP, Treister E, et al. 2004. *AJ* 128:2048–2065
Bauer FE, Arévalo P, Walton DJ, Koss MJ, Puccetti S, et al. 2015. *ApJ* 812:116
Berlind AA, Weinberg DH. 2002. *ApJ* 575:587–616
Bianchi S, Panessa F, Barcons X, Carrera FJ, La Franca F, et al. 2012. *MNRAS* 426:3225–3240
Bianchi S, Piconcelli E, Chiaberge M, Bailón EJ, Matt G, Fiore F. 2009. *ApJ* 695:781–787
Blecha L, Snyder GF, Satyapal S, Ellison SL. 2017. *ArXiv e-prints*
Bower RG, Benson AJ, Malbon R, Helly JC, Frenk CS, et al. 2006. *MNRAS* 370:645–655
Brandt WN, Alexander DM. 2015. *A&A Rev.* 23:1
Brightman M, Nandra K. 2011. *MNRAS* 413:1206–1235
Brocklehurst M. 1971. *MNRAS* 153:471–490

Buchanan CL, Gallimore JF, O'Dea CP, Baum SA, Axon DJ, et al. 2006. *AJ* 132:401–419
Buchner J, Bauer FE. 2017. *MNRAS* 465:4348–4362
Buchner J, Georgakakis A, Nandra K, Brightman M, Menzel ML, et al. 2015. *ApJ* 802:89
Bundy K, Bershady MA, Law DR, Yan R, Drory N, et al. 2015. *ApJ* 798:7
Burlon D, Ajello M, Greiner J, Comastri A, Merloni A, Gehrels N. 2011. *ApJ* 728:58–+
Burtscher L, Davies RI, Graciá-Carpio J, Koss MJ, Lin MY, et al. 2016. *A&A* 586:A28
Burtscher L, Meisenheimer K, Tristram KRW, Jaffe W, Hönig SF, et al. 2013. *A&A* 558:A149
Calzetti D, Kinney AL, Storchi-Bergmann T. 1994. *ApJ* 429:582–601
Carilli CL, Walter F. 2013. *ARA&A* 51:105–161
Chen CTJ, Hickox RC, Alberts S, Brodwin M, Jones C, et al. 2013. *ApJ* 773:3
Chen CTJ, Hickox RC, Alberts S, Harrison CM, Alexander DM, et al. 2015. *ApJ* 802:50
Cisternas M, Jahnke K, Bongiorno A, Inskip KJ, Impey CD, et al. 2011. *ApJ* 741:L11
Comastri A. 2004. *Compton-Thick AGN: The Dark Side of the X-Ray Background*. In *Supermassive Black Holes in the Distant Universe*, ed. AJ Barger, vol. 308 of *Astrophysics and Space Science Library*
Comastri A, Gilli R, Marconi A, Risaliti G, Salvati M. 2015. *A&A* 574:L10
Condon JJ. 1992. *ARA&A* 30:575–611
Croom SM, Lawrence JS, Bland-Hawthorn J, Bryant JJ, Fogarty L, et al. 2012. *MNRAS* 421:872–893
Davies RI, Burtscher L, Rosario D, Storchi-Bergmann T, Contursi A, et al. 2015. *ApJ* 806:127
Davies RI, Maciejewski W, Hicks EKS, Tacconi LJ, Genzel R, Engel H. 2009. *ApJ* 702:114–128
de Grijp MHK, Miley GK, Lub J, de Jong T. 1985. *Nature* 314:240–242
de Jong RS, Barden S, Bellido-Tirado O, Brynnel J, Chiappini C, et al. 2014. *4MOST: 4-metre Multi-Object Spectroscopic Telescope*. In *Society of Photo-Optical Instrumentation Engineers (SPIE) Conference Series*, vol. 9147 of *Society of Photo-Optical Instrumentation Engineers (SPIE) Conference Series*
Del Moro A, Alexander DM, Bauer FE, Daddi E, Kocevski DD, et al. 2016. *MNRAS* 456:2105–2125
Del Moro A, Alexander DM, Mullaney JR, Daddi E, Pannella M, et al. 2013. *A&A* 549:A59
Delvecchio I, Gruppioni C, Pozzi F, Berta S, Zamorani G, et al. 2014. *MNRAS* 439:2736–2754
Denney KD, De Rosa G, Croxall K, Gupta A, Bentz MC, et al. 2014. *ApJ* 796:134
DESI Collaboration, Aghamousa A, Aguilar J, Ahlen S, Alam S, et al. 2016. *(arXiv:1611.00036)*
Di Matteo T, Springel V, Hernquist L. 2005. *Nature* 433:604–607
Diamond-Stanic AM, Rieke GH. 2012. *ApJ* 746:168
DiPompeo MA, Hickox RC, Eftekharzadeh S, Myers AD. 2017a. *MNRAS* 469:4630–4643
DiPompeo MA, Hickox RC, Myers AD, Geach JE. 2017b. *MNRAS* 464:3526–3535
DiPompeo MA, Hickox RC, Runnoe JC, Carroll CM, Mullaney JR, Fischer TC. 2018. *ApJ submitted*
DiPompeo MA, Myers AD, Hickox RC, Geach JE, Hainline KN. 2014. *MNRAS* 442:3443–3453
DiPompeo MA, Myers AD, Hickox RC, Geach JE, Holder G, et al. 2015. *MNRAS* 446:3492–3501
Done C. 2010. *(arXiv:1008.2287)*
Done C, Gierliński M, Kubota A. 2007. *A&A Rev.* 15:1–66
Donley JL, Rieke GH, Rigby JR, Pérez-González PG. 2005. *ApJ* 634:169–182
Donoso E, Yan L, Tsai C, Eisenhardt P, Stern D, et al. 2012. *ApJ* 748:80
Draine BT. 2003a. *ARA&A* 41:241–289
Draine BT. 2003b. *ARA&A* 41:241–289
Draine BT, Lee HM. 1984. *ApJ* 285:89–108
Dubois Y, Peirani S, Pichon C, Devriendt J, Gavazzi R, et al. 2016. *MNRAS* 463:3948–3964
Elitzur M. 2012. *ApJ* 747:L33
Elitzur M, Ho LC. 2009. *ApJ* 701:L91–L94
Elitzur M, Netzer H. 2016. *MNRAS* 459:585–594
Ellison SL, Mendel JT, Patton DR, Scudder JM. 2013. *MNRAS* 435:3627–3638
Esquej P, Alonso-Herrero A, González-Martín O, Hönig SF, Hernán-Caballero A, et al. 2014. *ApJ*

780:86
Fabbiano G. 2006. *ARA&A* 44:323–366
Fabbiano G, Elvis M, Paggi A, Karovska M, Maksym WP, et al. 2017. *ApJ* 842:L4
Fabian AC. 2012. *ARA&A* 50:455–489
Fabian AC, Iwasawa K. 1999. *MNRAS* 303:L34–L36
Fabian AC, Vasudevan RV, Gandhi P. 2008. *MNRAS* 385:L43–L47
Fan L, Han Y, Fang G, Gao Y, Zhang D, et al. 2016. *ApJ* 822:L32
Farrah D, Afonso J, Efstathiou A, Rowan-Robinson M, Fox M, Clements D. 2003. *MNRAS* 343:585–607
Farrah D, Petty S, Connolly B, Blain A, Efstathiou A, et al. 2017. *ApJ* 844:106
Feruglio C, Fiore F, Carniani S, Piconcelli E, Zappacosta L, et al. 2015. *A&A* 583:A99
Fischer TC, Crenshaw DM, Kraemer SB, Schmitt HR. 2013. *ApJS* 209:1
Fritz J, Franceschini A, Hatziminaoglou E. 2006. *MNRAS* 366:767–786
Gabor JM, Bournaud F. 2013. *MNRAS* 434:606–620
Gallimore JF, Elitzur M, Maiolino R, Marconi A, O'Dea CP, et al. 2016. *ApJ* 829:L7
Gallo E, Treu T, Marshall PJ, Woo JH, Leipski C, Antonucci R. 2010. *ApJ* 714:25–36
Gandhi P, Horst H, Smette A, Hönig S, Comastri A, et al. 2009. *A&A* 502:457–472
Gao Y, Solomon PM. 2004. *ApJS* 152:63–80
García-Bernete I, Ramos Almeida C, Acosta-Pulido JA, Alonso-Herrero A, González-Martín O, et al. 2016. *MNRAS* 463:3531–3555
García-Burillo S, Combes F, Ramos Almeida C, Usero A, Krips M, et al. 2016. *ApJ* 823:L12
Gaskell CM. 2017. *MNRAS* 467:226–238
Genzel R, Lutz D, Sturm E, Egami E, Kunze D, et al. 1998. *ApJ* 498:579–605
Georgantopoulos I, Dasyra KM, Rovilos E, Pope A, Wu Y, et al. 2011. *A&A* 531:A116
Giacconi R. 2009. *Experimental Astronomy* 25:143–156
Gilli R, Comastri A, Hasinger G. 2007. *A&A* 463:79–96
Gilli R, Vignali C, Mignoli M, Iwasawa K, Comastri A, Zamorani G. 2010. *A&A* 519:A92+
Glikman E, Helfand DJ, White RL, Becker RH, Gregg MD, Lacy M. 2007. *ApJ* 667:673–703
Glikman E, Simmons B, Mailly M, Schawinski K, Urry CM, Lacy M. 2015. *ApJ* 806:218
Gohil R, Ballantyne DR. 2017. *MNRAS* 468:4944–4955
Goulding AD, Alexander DM. 2009. *MNRAS* 398:1165–1193
Goulding AD, Alexander DM, Bauer FE, Forman WR, Hickox RC, et al. 2012. *ApJ* 755:5
Goulding AD, Greene JE, Bezanson R, Greco J, Johnson S, et al. 2017. *PASJ submitted (arXiv:1706.07436)*
Graham AW. 2016. *Galaxy Bulges and Their Massive Black Holes: A Review*. In *Galactic Bulges*, eds. E Laurikainen, R Peletier, D Gadotti, vol. 418 of *Astrophysics and Space Science Library*
Greene JE, Zakamska NL, Ho LC, Barth AJ. 2011. *ApJ* 732:9
Hainline KN, Hickox R, Greene JE, Myers AD, Zakamska NL. 2013. *ApJ* 774:145
Hainline KN, Hickox RC, Greene JE, Myers AD, Zakamska NL, et al. 2014. *ApJ* 787:65
Hainline KN, Reines AE, Greene JE, Stern D. 2016. *ApJ* 832:119
Hao L, Weedman DW, Spoon HWW, Marshall JA, Levenson NA, et al. 2007. *ApJ* 655:L77–L80
Harrison C. 2014. *Observational constraints on the influence of active galactic nuclei on the evolution of galaxies*. Ph.D. thesis, Durham University
Harrison CM. 2017. *Nature Astronomy* 1:0165
Harrison CM, Alexander DM, Mullaney JR, Swinbank AM. 2014. *MNRAS* 441:3306–3347
Harrison FA, Aird J, Civano F, Lansbury G, Mullaney JR, et al. 2016. *ApJ* 831:185
Hasinger G. 2008. *A&A* 490:905–922
Hatziminaoglou E, Hernán-Caballero A, Feltre A, Piñol Ferrer N. 2015. *ApJ* 803:110
Heckman TM. 1980. *A&A* 87:152–164
Heckman TM, Best PN. 2014. *ARA&A* 52:589–660
Helou G, Soifer BT, Rowan-Robinson M. 1985. *ApJ* 298:L7–L11

Hickox RC, Jones C, Forman WR, Murray SS, Brodwin M, et al. 2007. *ApJ* 671:1365–1387
Hickox RC, Jones C, Forman WR, Murray SS, Kochanek CS, et al. 2009. *ApJ* 696:891–919
Hickox RC, Markevitch M. 2006. *ApJ* 645:95–114
Hickox RC, Myers AD, Brodwin M, Alexander DM, Forman WR, et al. 2011. *ApJ* 731:117–+
Hickox RC, Myers AD, Greene JE, Hainline KN, Zakamska NL, DiPompeo MA. 2017. *ApJ* 849:53
Hildebrand RH. 1983. *QJRAS* 24:267
Ho LC. 2008. *ARA&A* 46:475–539
Ho LC. 2009. *ApJ* 699:638–648
Ho LC, Filippenko AV, Sargent WLW. 1997. *ApJS* 112:315–+
Ho LC, Kim M, Terashima Y. 2012. *ApJ* 759:L16
Hönig SF, Kishimoto M. 2017. *ApJ* 838:L20
Hönig SF, Kishimoto M, Antonucci R, Marconi A, Prieto MA, et al. 2012. *ApJ* 755:149
Hönig SF, Kishimoto M, Gandhi P, Smette A, Asmus D, et al. 2010. *A&A* 515:A23
Hopkins PF, Hernquist L, Cox TJ, Kereš D. 2008. *ApJS* 175:356–389
Hopkins PF, Torrey P, Faucher-Giguère CA, Quataert E, Murray N. 2016. *MNRAS* 458:816–831
Humphrey A, Villar-Martín M, Ramos Almeida C, Tadhunter CN, Arribas S, et al. 2015. *MNRAS* 454:4452–4466
Hviding RE, Hickox RC, Hainline KN, Carroll CM, DiPompeo MA, et al. 2018. *MNRAS in press (1711.01269)*
Imanishi M, Dudley CC, Maiolino R, Maloney PR, Nakagawa T, Risaliti G. 2007. *ApJS* 171:72–100
Imanishi M, Nakanishi K, Izumi T. 2016. *AJ* 152:218
Ishibashi W, Fabian AC. 2016. *MNRAS* 463:1291–1296
Ishibashi W, Fabian AC. 2017. *MNRAS* 472:2768–2772
Jones ML, Hickox RC, Mutch SJ, Croton DJ, Ptak AF, DiPompeo MA. 2017. *ApJ* 843:125
Jud H, Schartmann M, Mould J, Burtscher L, Tristram KRW. 2017. *MNRAS* 465:248–259
Juneau S, Bournaud F, Charlot S, Daddi E, Elbaz D, et al. 2014. *ApJ* 788:88
Juneau S, Dickinson M, Alexander DM, Salim S. 2011. *ApJ* 736:104–+
Kauffmann G, Heckman TM, Tremonti C, Brinchmann J, Charlot S, et al. 2003. *MNRAS* 346:1055–1077
Kelly BC, Vestergaard M, Fan X, Hopkins P, Hernquist L, Siemiginowska A. 2010. *ApJ* 719:1315–1334
Kerr RP. 1963. *Physical Review Letters* 11:237–238
Kewley LJ, Dopita MA, Leitherer C, Davé R, Yuan T, et al. 2013. *ApJ* 774:100
Kewley LJ, Groves B, Kauffmann G, Heckman T. 2006. *MNRAS* 372:961–976
Khachikian EY, Weedman DW. 1974. *ApJ* 192:581–589
Kocevski DD, Brightman M, Nandra K, Koekemoer AM, Salvato M, et al. 2015. *ApJ* 814:104
Kocevski DD, Faber SM, Mozena M, Koekemoer AM, Nandra K, et al. 2012. *ApJ* 744:148
Kormendy J, Ho LC. 2013. *ARA&A* 51:511–653
Koss M, Mushotzky R, Veilleux S, Winter L. 2010. *ApJ* 716:L125–L130
Koss M, Trakhtenbrot B, Ricci C, Lamperti I, Oh K, et al. 2017. *ApJ in press (arXiv:1707.08123)*
Koss MJ, Assef R, Baloković M, Stern D, Gandhi P, et al. 2016. *ApJ* 825:85
LaMassa SM, Cales S, Moran EC, Myers AD, Richards GT, et al. 2015. *ApJ* 800:144
Lansbury GB, Alexander DM, Aird J, Gandhi P, Stern D, et al. 2017. *ApJ* 846:20
Lansbury GB, Gandhi P, Alexander DM, Assef RJ, Aird J, et al. 2015. *ApJ* 809:115
Lawrence A. 1991. *MNRAS* 252:586–592
Lehmer BD, Alexander DM, Bauer FE, Brandt WN, Goulding AD, et al. 2010. *ApJ* 724:559–571
Lehmer BD, Basu-Zych AR, Mineo S, Brandt WN, Eufrasio RT, et al. 2016. *ApJ* 825:7
Levenson NA, Heckman TM, Krolik JH, Weaver KA, Życki PT. 2006. *ApJ* 648:111–127
Levenson NA, Krolik JH, Życki PT, Heckman TM, Weaver KA, et al. 2002. *ApJ* 573:L81–L84
Liu G, Zakamska NL, Greene JE, Nesvadba NPH, Liu X. 2013. *MNRAS* 430:2327–2345
López-Gonzaga N, Burtscher L, Tristram KRW, Meisenheimer K, Schartmann M. 2016. *A&A*

591:A47
Low FJ, Cutri RM, Huchra JP, Kleinmann SG. 1988. *ApJ* 327:L41–L45
Luo B, Brandt WN, Xue YQ, Lehmer B, Alexander DM, et al. 2017. *ApJS* 228:2
Lusso E, Hennawi JF, Comastri A, Zamorani G, Richards GT, et al. 2013. *ApJ* 777:86
Lusso E, Risaliti G. 2016. *ApJ* 819:154
Lutz D. 2014. *ARA&A* 52:373–414
MacLeod CL, Ross NP, Lawrence A, Goad M, Horne K, et al. 2016. *MNRAS* 457:389–404
Madau P, Dickinson M. 2014. *ARA&A* 52:415–486
Maiolino R, Shemmer O, Imanishi M, Netzer H, Oliva E, et al. 2007. *A&A* 468:979–992
Malizia A, Bassani L, Bazzano A, Bird AJ, Masetti N, et al. 2012. *MNRAS* 426:1750–1766
Marin F, Dovčiak M, Muleri F, Kislat FF, Krawczynski HS. 2018. *MNRAS* 473:1286–1316
Martínez-Sansigre A, Taylor AM. 2009. *ApJ* 692:964–972
Mateos S, Alonso-Herrero A, Carrera FJ, Blain A, Watson MG, et al. 2012. *MNRAS* 426:3271–3281
Mateos S, Carrera FJ, Alonso-Herrero A, Hernán-Caballero A, Barcons X, et al. 2016. *ApJ* 819:166
Mateos S, Carrera FJ, Barcons X, Alonso-Herrero A, Hernán-Caballero A, et al. 2017. *ApJ* 841:L18
Matt G, Guainazzi M, Maiolino R. 2003. *MNRAS* 342:422–426
Mayer L, Kazantzidis S, Escala A, Callegari S. 2010. *Nature* 466:1082–1084
McAlpine S, Bower RG, Harrison CM, Crain RA, Schaller M, et al. 2017. *MNRAS* 468:3395–3407
McConnell NJ, Ma CP. 2013. *ApJ* 764:184
McDermid RM, Alatalo K, Blitz L, Bournaud F, Bureau M, et al. 2015. *MNRAS* 448:3484–3513
Mendez AJ, Coil AL, Aird J, Skibba RA, Diamond-Stanic AM, et al. 2016. *ApJ* 821:55
Merloni A, Bongiorno A, Brusa M, Iwasawa K, Mainieri V, et al. 2014. *MNRAS* 437:3550–3567
Merloni A, Heinz S. 2008. *MNRAS* 388:1011–1030
Merloni A, Predehl P, Becker W, Böhringer H, Boller T, et al. 2012. *eROSITA Science Book: Mapping the Structure of the Energetic Universe (arXiv:1209.3114)*
Mignoli M, Vignali C, Gilli R, Comastri A, Zamorani G, et al. 2013. *A&A* 556:A29
Mineo S, Gilfanov M, Sunyaev R. 2012. *MNRAS* 419:2095–2115
Mingozzi M, Vallini L, Pozzi F, Vignali C, Mignano A, et al. 2018. *MNRAS* 474:3640–3648
Miniutti G, Saxton RD, Rodríguez-Pascual PM, Read AM, Esquej P, et al. 2013. *MNRAS* 433:1764–1777
Moran EC, Barth AJ, Eracleous M, Kay LE. 2007. *ApJ* 668:L31–L34
Mortlock DJ, Warren SJ, Venemans BP, Patel M, Hewett PC, et al. 2011. *Nature* 474:616–619
Moss VA, Allison JR, Sadler EM, Urquhart R, Soria R, et al. 2017. *MNRAS* 471:2952–2973
Mullaney JR, Daddi E, Béthermin M, Elbaz D, Juneau S, et al. 2012. *ApJ* 753:L30
Murphy KD, Yaqoob T. 2009. *MNRAS* 397:1549–1562
Mushotzky RF, Done C, Pounds KA. 1993. *ARA&A* 31:717–761
Natarajan P, Pacucci F, Ferrara A, Agarwal B, Ricarte A, et al. 2017. *ApJ* 838:117
Negri A, Volonteri M. 2017. *MNRAS* 467:3475–3492
Nenkova M, Sirocky MM, Nikutta R, Ivezić Ž, Elitzur M. 2008. *ApJ* 685:160–180
Netzer H. 2015. *ARA&A* 53:365–408
Novak GS. 2013. *MNRAS submitted (arXiv:1310.3833)*
Osterbrock DE. 1981. *ApJ* 249:462–470
Ostorero L, Morganti R, Diaferio A, Siemiginowska A, Stawarz Ł, et al. 2016. *Astronomische Nachrichten* 337:148
Padovani P. 2016. *A&A Rev.* 24:13
Padovani P, Alexander DM, Assef RJ, De Marco B, Giommi P, et al. 2017. *A&A Rev.* 25:2
Page MJ, Carrera FJ, Stevens JA, Ebrero J, Blustin AJ. 2011. *MNRAS* 416:2792–2801
Page MJ, Stevens JA, Ivison RJ, Carrera FJ. 2004. *ApJ* 611:L85–L88
Panessa F, Bassani L. 2002. *A&A* 394:435–442
Park T, Kashyap VL, Siemiginowska A, van Dyk DA, Zezas A, et al. 2006. *submitted to ApJ, astro-ph/0606247*

Peeters E, Spoon HWW, Tielens AGGM. 2004. *ApJ* 613:986–1003
Pereira-Santaella M, Diamond-Stanic AM, Alonso-Herrero A, Rieke GH. 2010. *ApJ* 725:2270–2280
Pope A, Chary RR, Alexander DM, Armus L, Dickinson M, et al. 2008. *ApJ* 675:1171–1193
Predehl P, Schmitt JHMM. 1995. *A&A* 293:889–905
Raban D, Jaffe W, Röttgering H, Meisenheimer K, Tristram KRW. 2009. *MNRAS* 394:1325–1337
Ramos Almeida C, Levenson NA, Alonso-Herrero A, Asensio Ramos A, Rodríguez Espinosa JM, et al. 2011. *ApJ* 731:92
Ramos Almeida C, Martínez González MJ, Asensio Ramos A, Acosta-Pulido JA, Hönig SF, et al. 2016. *MNRAS* 461:1387–1403
Ramos Almeida C, Ricci C. 2017. *Nature Astronomy* 1:679–689
Rees MJ. 1984. *ARA&A* 22:471–506
Revnivtsev M, Churazov E, Sazonov S, Forman W, Jones C. 2008. *A&A* 490:37–43
Ricci C, Bauer FE, Treister E, Schawinski K, Privon GC, et al. 2017a. *MNRAS* 468:1273–1299
Ricci C, Trakhtenbrot B, Koss MJ, Ueda Y, Del Vecchio I, et al. 2017b. *ApJS in press (arXiv:1709.03989)*
Ricci C, Trakhtenbrot B, Koss MJ, Ueda Y, Schawinski K, et al. 2017c. *Nature* 549:488–491
Ricci C, Ueda Y, Koss MJ, Trakhtenbrot B, Bauer FE, Gandhi P. 2015. *ApJ* 815:L13
Richards GT, Fan X, Schneider DP, Vanden Berk DE, Strauss MA, et al. 2001. *AJ* 121:2308–2330
Risaliti G, Elvis M, Fabbiano G, Baldi A, Zezas A. 2005. *ApJ* 623:L93–L96
Risaliti G, Elvis M, Nicastro F. 2002. *ApJ* 571:234–246
Roche PF, Packham C, Telesco CM, Radomski JT, Alonso-Herrero A, et al. 2006. *MNRAS* 367:1689–1698
Rosario DJ, Santini P, Lutz D, Shao L, Maiolino R, et al. 2012. *A&A* 545:A45
Rosenberg MJF, van der Werf PP, Aalto S, Armus L, Charmandaris V, et al. 2015. *ApJ* 801:72
Rybicki GB, Lightman AP. 1986. *Radiative Processes in Astrophysics*
Sajina A, Yan L, Fadda D, Dasyra K, Huynh M. 2012. *ApJ* 757:13
Sánchez SF, Kennicutt RC, Gil de Paz A, van de Ven G, Vílchez JM, et al. 2012. *A&A* 538:A8
Sanders DB, Mirabel IF. 1996. *ARA&A* 34:749
Sanders DB, Soifer BT, Elias JH, Madore BF, Matthews K, et al. 1988. *ApJ* 325:74–91
Satyapal S, Ellison SL, McAlpine W, Hickox RC, Patton DR, Mendel JT. 2014. *MNRAS* 441:1297–1304
Satyapal S, Vega D, Dudik RP, Abel NP, Heckman T. 2008. *ApJ* 677:926–942
Schartmann M, Wada K, Prieto MA, Burkert A, Tristram KRW. 2014. *MNRAS* 445:3878–3891
Schawinski K, Treister E, Urry CM, Cardamone CN, Simmons B, Yi SK. 2011. *ApJ* 727:L31+
Schawinski K, Urry CM, Virani S, Coppi P, Bamford SP, et al. 2010. *ApJ* 711:284–302
Schmidt M. 1963. *Nature* 197:1040
Schnorr-Müller A, Davies RI, Korista KT, Burtscher L, Rosario D, et al. 2016. *MNRAS* 462:3570–3590
Seyfert CK. 1943. *ApJ* 97:28
Shakura NI, Sunyaev RA. 1973. *A&A* 24:337–355
Shapiro SL, Teukolsky SA. 1983. *Black holes, white dwarfs, and neutron stars: The physics of compact objects*. New York: Wiley-Interscience
She R, Ho LC, Feng H. 2017. *ApJ* 835:223
Shi Y, Helou G, Armus L, Stierwalt S, Dale D. 2013. *ApJ* 764:28
Shi Y, Rieke GH, Hines DC, Gorjian V, Werner MW, et al. 2006. *ApJ* 653:127–136
Siebenmorgen R, Haas M, Pantin E, Krügel E, Leipski C, et al. 2008. *A&A* 488:83–90
Siebenmorgen R, Heymann F, Efstathiou A. 2015. *A&A* 583:A120
Simpson C. 2005. *MNRAS* 360:565–572
Smith JDT, Draine BT, Dale DA, Moustakas J, Kennicutt Jr. RC, et al. 2007. *ApJ* 656:770–791
Soltan A. 1982. *MNRAS* 200:115–122
Spinoglio L, Malkan MA. 1992. *ApJ* 399:504–520

Stalevski M, Fritz J, Baes M, Nakos T, Popović LČ. 2012. *MNRAS* 420:2756–2772
Stalevski M, Ricci C, Ueda Y, Lira P, Fritz J, Baes M. 2016. *MNRAS* 458:2288–2302
Stanley F, Harrison CM, Alexander DM, Swinbank AM, Aird JA, et al. 2015. *MNRAS* 453:591–604
Steffen AT, Strateva I, Brandt WN, Alexander DM, Koekemoer AM, et al. 2006. *AJ* 131:2826–2842
Stern D, Eisenhardt P, Gorjian V, Kochanek CS, Caldwell N, et al. 2005. *ApJ* 631:163–168
Stern D, Lansbury GB, Assef RJ, Brandt WN, Alexander DM, et al. 2014. *ApJ* 794:102
Suganuma M, Yoshii Y, Kobayashi Y, Minezaki T, Enya K, et al. 2006. *ApJ* 639:46–63
Tadhunter C. 2016. *A&A Rev.* 24:10
Takada M, Ellis RS, Chiba M, Greene JE, Aihara H, et al. 2014. *PASJ* 66:1
Thompson TA, Quataert E, Murray N. 2005. *ApJ* 630:167–185
Tielens AGGM. 2008. *ARA&A* 46:289–337
Toba Y, Oyabu S, Matsuhara H, Malkan MA, Gandhi P, et al. 2014. *ApJ* 788:45
Tran HD. 2003. *ApJ* 583:632–648
Treister E, Krolik JH, Dullemond C. 2008. *ApJ* 679:140–148
Treister E, Schawinski K, Urry CM, Simmons BD. 2012. *ApJ* 758:L39
Treister E, Urry CM, Virani S. 2009. *ApJ* 696:110–120
Tristram KRW, Burtscher L, Jaffe W, Meisenheimer K, Hönig SF, et al. 2014. *A&A* 563:A82
Trouille L, Barger AJ, Tremonti C. 2011. *ApJ* 742:46
Trump JR, Impey CD, Kelly BC, Civano F, Gabor JM, et al. 2011. *ApJ* 733:60
Ueda Y, Akiyama M, Hasinger G, Miyaji T, Watson MG. 2014. *ApJ* 786:104
Urry CM, Padovani P. 1995. *PASP* 107:803
Vanden Berk DE, Richards GT, Bauer A, Strauss MA, Schneider DP, et al. 2001. *AJ* 122:549–564
Vazquez B, Galianni P, Richmond M, Robinson A, Axon DJ, et al. 2015. *ApJ* 801:127
Veilleux S, Osterbrock DE. 1987. *ApJS* 63:295–310
Vergani D, Garilli B, Polletta M, Franzetti P, Scodeggio M, et al. 2018. *A&A submitted (arXiv:1712.08168)*
Vignali C, Alexander DM, Gilli R, Pozzi F. 2010. *MNRAS* 404:48–59
Villar-Martín M, Arribas S, Emonts B, Humphrey A, Tadhunter C, et al. 2016. *MNRAS* 460:130–162
Villforth C, Hamilton T, Pawlik MM, Hewlett T, Rowlands K, et al. 2017. *MNRAS* 466:812–830
Vito F, Brandt WN, Yang G, Gilli R, Luo B, et al. 2018. *MNRAS* 473:2378–2406
Volonteri M. 2010. *A&A Rev.* 18:279–315
Volonteri M, Begelman MC. 2010. *MNRAS* 409:1022–1032
Wada K, Schartmann M, Meijerink R. 2016. *ApJ* 828:L19
Wang SX, Brandt WN, Luo B, Smail I, Alexander DM, et al. 2013. *ApJ* 778:179
Ward MJ, Geballe T, Smith M, Wade R, Williams P. 1987. *ApJ* 316:138–144
Webster RL, Francis PJ, Peterson BA, Drinkwater MJ, Masci FJ. 1995. *Nature* 375:469
Weedman DW. 1977. *ARA&A* 15:69–95
Weigel AK, Schawinski K, Caplar N, Wong OI, Treister E, Trakhtenbrot B. 2017. *ApJ* 845:134
Weinberger R, Springel V, Hernquist L, Pillepich A, Marinacci F, et al. 2017. *MNRAS* 465:3291–3308
Weston ME, McIntosh DH, Brodwin M, Mann J, Cooper A, et al. 2017. *MNRAS* 464:3882–3906
Wilkes BJ, Kuraszkiewicz J, Haas M, Barthel P, Leipski C, et al. 2013. *ApJ* 773:15
Wilms J, Allen A, McCray R. 2000. *ApJ* 542:914–924
Wu XB, Wang F, Fan X, Yi W, Zuo W, et al. 2015. *Nature* 518:512–515
Xue YQ, Luo B, Brandt WN, Bauer FE, Lehmer BD, et al. 2011. *ApJS* 195:10–+
Yan R, Ho LC, Newman JA, Coil AL, Willmer CNA, et al. 2011. *ApJ* 728:38–+
Yu Q, Tremaine S. 2002. *MNRAS* 335:965–976
Yuan F, Narayan R. 2014. *ARA&A* 52:529–588
Zakamska NL, Strauss MA, Krolik JH, Collinge MJ, Hall PB, et al. 2003. *AJ* 126:2125–2144
Zakamska NL, Strauss MA, Krolik JH, Ridgway SE, Schmidt GD, et al. 2006. *AJ* 132:1496–1516

Zhu G, Blanton MR, Moustakas J. 2010. *ApJ* 722:491–519